2015

The Q(weak) experimental apparatus

T. Allison

J. Beaufait

J. Benesch

D. S. Armstrong
College of William and Mary

T. Averett
College of William and Mary

See next page for additional authors

Recommended Citation

Allison, T., Anderson, M., Androić, D., Armstrong, D. S., Asaturyan, A., Averett, T., ... & Benesch, J. (2015). The Qweak experimental apparatus. Nuclear Instruments and Methods in Physics Research Section A: Accelerators, Spectrometers, Detectors and Associated Equipment, 781, 105-133.

Nuclear Instruments and Methods in Physics Research A 781 (2015) 105–133

Contents lists available at ScienceDirect

Nuclear Instruments and Methods in Physics Research A

journal homepage: www.elsevier.com/locate/nima

The Q_{weak} experimental apparatus

T. Allison [a], M. Anderson [b,1], D. Androić [c], D.S. Armstrong [d], A. Asaturyan [e], T. Averett [d], R. Averill [f], J. Balewski [f], J. Beaufait [a], R.S. Beminiwattha [g], J. Benesch [a], F. Benmokhtar [h,2], J. Bessuille [i,3], J. Birchall [b], E. Bonnell [j], J.D. Bowman [k], P. Brindza [a], D.B. Brown [l], R.D. Carlini [a,d], G.D. Cates [m], B. Cavness [n], G. Clark [i], J.C. Cornejo [d], S. Covrig Dusa [a], M.M. Dalton [m,4], C.A. Davis [i], D.C. Dean [d], W. Deconinck [d], J. Diefenbach [o], K. Dow [f], J.F. Dowd [d], J.A. Dunne [l], D. Dutta [l], W.S. Duvall [j], J.R. Echols [j], M. Elaasar [p], W.R. Falk [b], K.D. Finelli [j], J.M. Finn [d,5], D. Gaskell [a], M.T.W. Gericke [b], J. Grames [a], V.M. Gray [d], K. Grimm [d,q,6], F. Guo [f], J. Hansknecht [a], D.J. Harrison [r], E. Henderson [d], J.R. Hoskins [d], E. Ihloff [f], K. Johnston [q], D. Jones [m], M. Jones [a], R. Jones [s], M. Kargiantoulakis [m], J. Kelsey [f], N. Khan [i], P.M. King [g], E. Korkmaz [t], S. Kowalski [f], A. Kubera [u], J. Leacock [j], J.P. Leckey [d,7], A.R. Lee [j], J.H. Lee [g,d,8], L. Lee [i,b], Y. Liang [v], S. MacEwan [b], D. Mack [a], J.A. Magee [d], R. Mahurin [b,9], J. Mammei [j,b,10], J.W. Martin [r], A. McCreary [x], M.H. McDonald [r], M.J. McHugh [v], P. Medeiros [a], D. Meekins [a], J. Mei [a,11], R. Michaels [a], A. Micherdzinska [v], A. Mkrtchyan [e], H. Mkrtchyan [e], N. Morgan [j], J. Musson [a], K.E. Mesick [v,12], A. Narayan [l], L.Z. Ndukum [l], V. Nelyubin [m], Nuruzzaman [o,l], W.T.H. van Oers [b,i], A.K. Opper [v], S.A. Page [b], J. Pan [b], K.D. Paschke [m], S.K. Phillips [w], M.L. Pitt [j], M. Poelker [a], J.F. Rajotte [f], W.D. Ramsay [i,b], W.R. Roberts [i], J. Roche [g], P.W. Rose [d], B. Sawatzky [a], T. Seva [c], M.H. Shabestari [l], R. Silwal [m,3], N. Simicevic [q], G.R. Smith [a,*], S. Sobczynski [f], P. Solvignon [a], D.T. Spayde [y], B. Stokes [v], D.W. Storey [r], A. Subedi [l], R. Subedi [v], R. Suleiman [a], V. Tadevosyan [e], W.A. Tobias [m], V. Tvaskis [r,b], E. Urban [y,13], B. Waidyawansa [g], P. Wang [b], S.P. Wells [q], S.A. Wood [a], S. Yang [d], S. Zhamkochyan [e], R.B. Zielinski [d]

[a] Thomas Jefferson National Accelerator Facility, Newport News, VA 23606, USA
[b] University of Manitoba, Winnipeg, MB, Canada R3T2N2
[c] University of Zagreb, Zagreb, HR 10002, Croatia
[d] College of William and Mary, Williamsburg, VA 23185, USA
[e] A. I. Alikhanyan National Science Laboratory (Yerevan Physics Institute), Yerevan 0036, Armenia
[f] Massachusetts Institute of Technology, Cambridge, MA 02139, USA
[g] Ohio University, Athens, OH 45701, USA
[h] Christopher Newport University, Newport News, VA 23606, USA
[i] TRIUMF, Vancouver, BC, Canada V6T2A3
[j] Virginia Polytechnic Institute & State University, Blacksburg, VA 24061, USA
[k] Los Alamos National Lab, Los Alamos, NM 87545, USA
[l] Mississippi State University, Mississippi State, MS 39762, USA
[m] University of Virginia, Charlottesville, VA 22903, USA
[n] Angelo State University, San Angelo, TX 76909, USA
[o] Hampton University, Hampton, VA 23668, USA
[p] Southern University at New Orleans, New Orleans, LA 70126, USA
[q] Louisiana Tech University, Ruston, LA 71272, USA
[r] University of Winnipeg, Winnipeg, MB, Canada R3B2E9
[s] University of Connecticut, Storrs-Mansfield, CT 06269, USA
[t] University of Northern British Columbia, Prince George, BC, Canada V2N4Z9
[u] Kent State University, Kent, OH 44240, USA
[v] George Washington University, Washington, DC 20052, USA
[w] University of New Hampshire, Durham, NH 03824, USA
[x] University of Pittsburgh, Pittsburgh, PA 15260, USA
[y] Hendrix College, Conway, AR 72032, USA

http://dx.doi.org/10.1016/j.nima.2015.01.023
0168-9002/

ARTICLE INFO

Article history:
Received 24 September 2014
Received in revised form
19 December 2014
Accepted 6 January 2015
Available online 14 January 2015

Keywords:
Parity violation
Electron scattering
High luminosity
Liquid hydrogen target
Particle detectors

ABSTRACT

The Jefferson Lab Q_{weak} experiment determined the weak charge of the proton by measuring the parity-violating elastic scattering asymmetry of longitudinally polarized electrons from an unpolarized liquid hydrogen target at small momentum transfer. A custom apparatus was designed for this experiment to meet the technical challenges presented by the smallest and most precise $\vec{e}$p asymmetry ever measured. Technical milestones were achieved at Jefferson Lab in target power, beam current, beam helicity reversal rate, polarimetry, detected rates, and control of helicity-correlated beam properties. The experiment employed 180 μA of 89% longitudinally polarized electrons whose helicity was reversed 960 times per second. The electrons were accelerated to 1.16 GeV and directed to a beamline with extensive instrumentation to measure helicity-correlated beam properties that can induce false asymmetries. Møller and Compton polarimetry were used to measure the electron beam polarization to better than 1%. The electron beam was incident on a 34.4 cm liquid hydrogen target. After passing through a triple collimator system, scattered electrons between 5.8° and 11.6° were bent in the toroidal magnetic field of a resistive copper-coil magnet. The electrons inside this acceptance were focused onto eight fused silica Cherenkov detectors arrayed symmetrically around the beam axis. A total scattered electron rate of about 7 GHz was incident on the detector array. The detectors were read out in integrating mode by custom-built low-noise pre-amplifiers and 18-bit sampling ADC modules. The momentum transfer $Q^2=0.025$ GeV^2 was determined using dedicated low-current ($\sim$100 pA) measurements with a set of drift chambers before (and a set of drift chambers and trigger scintillation counters after) the toroidal magnet.

1. Introduction

1.1. Motivation

The Q_{weak} experiment was designed [1] to perform the first determination [2] of the proton's weak charge, Q_w^p, which is the neutral-weak analog of the proton's electric charge. While measurement of this fundamental property of the proton is interesting in its own right, it can also be related [3] to the weak mixing angle $\sin^2\theta_{\text{w}}$ and will provide the most sensitive measure of the Q^2 evolution (running) of $\sin^2\theta_{\text{w}}$ below the Z-pole. As such it provides a sensitive test for new physics beyond the SM.[14] When combined with precise experiments on other targets, such as can be found in atomic parity-violating measurements on ^{133}Cs [4], the axial electron, vector quark coupling constants $C_{1i}=2g_A^e g_V^i$ can be extracted and used (for example) to form the weak charge of the neutron as well [2].

To accomplish these goals, a precise measure of the PVES[15] asymmetry A_{ep} from unpolarized hydrogen must be performed at low 4-momentum transfer squared ($-Q^2$). The asymmetry A_{ep} is the difference over the sum of elastic $\vec{e}\,p$ cross-sections measured with longitudinally polarized electrons of opposite helicity. After a small correction for the one energy-dependent electroweak radiative correction that contributes at forward angles [5], in the forward-angle limit the asymmetry can be cast in the simple form

$$A_{ep}/A_0 = Q_W^p + Q^2 F^p(Q^2,\theta) \tag{1}$$

where $A_0=-G_F Q^2/(4\pi\alpha\sqrt{2})$, G_F is the Fermi constant, and α is the fine structure constant. The second term Q^2F^p contains the nucleon structure defined in terms Q^2F^p of electromagnetic, neutral-weak, and axial form factors. F^p can be determined [6] from existing PVES data at modestly higher Q^2 [7–18], and is suppressed at lower Q^2 relative to Q_w^p by the additional factor of Q^2.

The strategy employed in the Q_{weak} experiment was to perform the most precise $\vec{e}\,p$ asymmetry measurement to date [2] at a Q^2 four times smaller than any previously reported $\vec{e}\,p$ experiment, to ensure a reliable (short) extrapolation to threshold where the intercept Q_w^p of Eq. (1) is the quantity of interest. As mentioned above, the nucleon structure term is also smaller at smaller Q^2. The fundamental challenge is that the expected SM asymmetry at the small Q^2 of the experiment (0.025 GeV^2) is only -230 ppb, and the proposed goal of a $\sim$2.5% asymmetry measurement implies that the experiment must achieve an overall uncertainty of scale 6 ppb. The small Q^2, small asymmetry, and ambitious uncertainty goal led to an experiment which pushed boundaries on many fronts, as described below.

1.2. Overview of the experiment

A custom apparatus (see Figs. 1 and 2) was built and installed in Hall C at JLab[16] [19] to provide the high luminosity, large acceptance, and systematic control required for the Q_{weak} experiment. Several improvements (see Section 2) were made in the accelerator's source and injector to meet the requirements of the experiment, which employed a 180 μA beam of 1.16 GeV, $\sim$89% longitudinally polarized electrons. Improvements to the beamline instrumentation were made in the polarized source and the Hall C beamline (see Section 3). The incident beam polarization was measured in two independent polarimeters (Section 4).

Electrons scattered from a 34.4 cm liquid hydrogen target (Section 5) were detected in eight synthetic quartz Cherenkov detectors each 200 cm $\times$ 18 cm $\times$ 1.25 cm thick (Section 8.1) arrayed in an azimuthally symmetric pattern about the beam axis, which covered 49% of 2π in the azimuthal angle ϕ. The eight-fold

* Corresponding author. Tel.: +1 757 269 5405.
E-mail address: smithg@jlab.org (G.R. Smith).
[1] Present address: ICMP, École Polytechnique Fédérale de Lausanne (EPFL), 1015 Lausanne, Switzerland.
[2] Present address: Duquesne University, Pittsburgh, PA 15282, USA.
[3] Present address: Massachusetts Institute of Technology, Cambridge, MA 02139, USA.
[4] Present address: Thomas Jefferson National Accelerator Facility, Newport News, VA 23606, USA.
[5] Deceased.
[6] Present address: Berthold Technologies, Bad Wildbad, Germany.
[7] Present address: Indiana University, Bloomington, IN 47405, USA.
[8] Present address: Institute for Basic Science, Daejeon, South Korea.
[9] Present address: Middle Tennessee State University, Murfreesboro, TN 37132, USA.
[10] Present address: University of Manitoba, Winnipeg, MB, Canada R3T2N2.
[11] Present address: CGG Veritas, Houston, TX 77081, USA.
[12] Present address: Rutgers, the State University of New Jersey, Piscataway, NJ 08854, USA.
[13] Present address: University of California, Berkeley, CA 94720, USA.
[14] Standard model.
[15] Parity-violating electron scattering.
[16] Thomas Jefferson National Accelerator Facility.

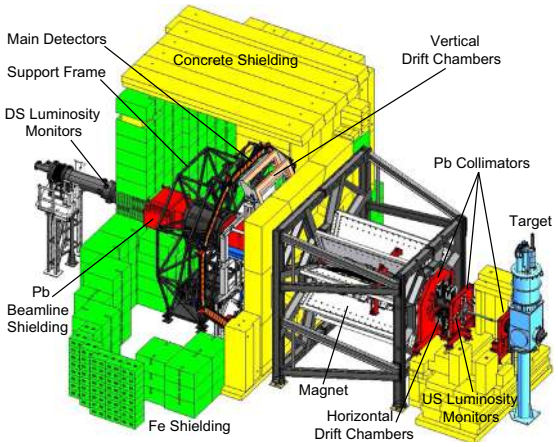

Fig. 1. CAD view of the experimental apparatus. The beam is incident from the right. The key elements include the liquid hydrogen target scattering chamber, a triple collimator system, a resistive eight-fold symmetric toroidal magnetic spectrometer, and eight Cherenkov detectors for the measurement of scattered electrons. Tracking chambers are illustrated just upstream of the Cherenkov detectors, as well as just upstream of the third collimator. Portions of the extensive steel and concrete shielding are also shown. The experiment had two operating modes: a low-current calibration mode for Q^2 acceptance mapping and background measurements, and a high-current production mode for the asymmetry measurement. The tracking detectors were only used during low current running (and were retracted during high current running).

azimuthal symmetry minimized and helped to characterize effects arising from HC[17] beam motion as well as residual transverse polarization in the beam. A carefully tailored triplet of lead collimators (Section 6.1) restricted the scattering angular acceptance to $5.8^\circ \le \theta \le 11.6^\circ$ and suppressed backgrounds. A resistive toroidal magnet (Section 7) between the target and the detectors separated the elastic electrons from inelastic and Møller electrons. In conjunction with the collimation system, the magnet also separated elastically scattered electrons from direct line-of-sight (neutral) events originating in the target.

A number of ancillary detectors helped to characterize backgrounds and establish HC beam properties in the experiment. A tracking system (Section 9) consisting of drift chambers before and after the magnet was deployed periodically to verify the acceptance-weighted central kinematics of the measurement, and to help study backgrounds. The electronics and data acquisition system are described in Section 10. The extensive simulations performed for the experiment, as well as the analysis scheme, are described in Section 11. The parameters of the experiment are summarized in Table 1.

1.3. Asymmetry considerations

The current from the PMT[18] at each end of the eight quartz Cherenkov detectors was read out, converted to a voltage, and digitized. The raw asymmetry measured for a given detector PMT is provided by the following expressions:

$$A_{\rm raw} = \frac{Y^+ - Y^-}{Y^+ + Y^-} \tag{2}$$

$$A_{\rm raw} = P\left(\frac{f_p}{R}A_{ep} + \sum_b f_b A_b\right) + A_{\rm beam} + A_T + A_\epsilon. \tag{3}$$

Here $Y^\pm$ is the integrated signal yield seen in a given PMT for a right-handed $(+)$ or left-handed $(-)$ electron beam helicity state, normalized to the measured beam charge. A_{ep} is the elastic $\vec{e}p$ asymmetry the experiment was designed to provide. The factors $f_p = 1 - \sum_b f_b$ and $f_b = \langle Y_b\rangle/\langle Y\rangle$ represent the fractional contributions (dilutions) of elastic ep events and background events to the total yield, respectively. P is the beam polarization, the A_b are various background asymmetries, and $A_{\rm beam} = A_{\rm beam}(E, X, Y, X', Y')$ is the false asymmetry due to HC changes in the beam properties. The latter includes yield changes due to beam position (X,Y), beam angle (X', Y'), and beam energy (E) on target. The beam charge asymmetry was reduced with an active feedback loop. A_T accounts for potential contributions from transverse polarization components in the nominally longitudinally polarized beam. The A_ϵ term accounts for electronic contributions from potential helicity signal leakage into the DAQ[19] electronics or the detector signal pedestal. As described in [2], the factor R accounts for small corrections due to the effects of bremsstrahlung, light variation and nonuniform Q^2 distribution across the detectors, the finite precision of the Q^2 determination, and transforming from $\langle A(Q^2)\rangle$ to $A(\langle Q^2\rangle)$.

Using Eq. (3) as a basis, the experiment was designed to make precise measurements of the beam polarization, the momentum transfer, and the scattered electron yield. The experiment was also designed to highly suppress backgrounds and HC electronic and beam effects. Components were included in the experiment to allow ancillary measurements of background asymmetries and yields, as well as HC beam properties.

The statistical accuracy $\Delta A/A$ achievable in the experiment can be expressed in terms of the asymmetry width σ_A measured over helicity quartets, the total number of helicity quartets N, the expected asymmetry A, and the beam polarization P according to

$$\frac{\Delta A}{A} = \frac{\sigma_A}{AP\sqrt{N}}. \tag{4}$$

Helicity quartets refer to the pattern of beam helicity states used in the experiment: either $(+--+)$ or $(-++-)$. Assuming an efficiency of 50%, and the helicity reversal rate of 960/s used in the experiment, N is about 10^7 quartets per day. The asymmetry width is the sum in quadrature of contributions from the statistics per quartet accumulated in the detectors (215 ppm corrected for the 70 μs helicity reversal switching time, 42 μs gate delay, and 10% detector resolution), the beam current monitor resolution ($\sim$43 ppm), and the width from noise (density fluctuations) in the liquid hydrogen target ($\sim$55 ppm). σ_A was typically 225–230 ppm in the experiment (see Fig. 3), and was dominated by counting statistics. Under these conditions 270 days are required to reach a statistical accuracy ΔA/A of 2.1%.

1.4. Beam helicity reversal

A crucial tool to suppress systematic effects and facilitate a clean extraction of the physics asymmetry in the $Q_{\rm weak}$ experiment was fast helicity reversal. Since the detector signals can, and do, fluctuate, the faster the helicity reversal, the more accurate is the description of the experimental apparatus as a linear measurement device. Possible signal changes include slow gain drifts, target density fluctuations, and beam drifts.

The performance of the Pockels cell used to reverse the beam helicity in the injector (see Section 2.2) was upgraded for the $Q_{\rm weak}$ experiment. The helicity switching time was reduced from 500 μs to 70 μs and the helicity reversal rate was increased from 30 to 960 per second. A quartet helicity reversal pattern was used to remove

[17] Helicity-correlated.
[18] Photo multiplier tube.
[19] Data acquisition.

Fig. 2. The Q_{weak} experimental apparatus during installation, before most of the equipment was covered with shielding. The target scattering chamber is on the left, followed by the first two lead collimators on either side of the man in the figure. A third lead collimator faced with aluminum sits just in front of the large frame in the center of the picture, which supports the eight magnet coils. Three of the eight quartz detector bars appear just downstream and to the right of the magnet as skinny, long bars.

Table 1
Typical parameters characterizing the second half of the experiment.

Quantity	Value
Beam energy	1.16 GeV
Beam polarization	89%
Target length	34.4 cm
Beam current	180 μA
Luminosity	1.7×10^{39} cm^{-2} s^{-1}
Beam power in target	2.1 kW
θ Acceptance	5.8–11.6°
ϕ Acceptance	49% of 2π
Q^2	0.025 GeV^2
$\Delta\Omega_{\text{elastic}}$	43 msr
$\int \mid \vec{B} \mid dl$	0.9 T m
Total detector rate	7 GHz

linear drifts in the detector signals, and the fast reversal made the approximation of relatively slow random fluctuations as linear drifts valid.

The asymmetry was calculated for each helicity quartet using Eq. (2). When averaged over long time periods the small remaining asymmetries due to non-linear drifts should have random signs and average out. Any remnant of these drifts and fluctuations (along with other sources of unwanted excess noise) would increase the width of the measured asymmetries. Therefore, the health and efficiency of the experiment can be assessed by examining the difference between the observed asymmetry width, and that expected from the sum in quadrature of counting statistics, the beam current monitors, and the target.

1.5. Logistics of the experiment

The experiment was performed in two very different modes. The primary measurement of the $\vec{e}\,p$ asymmetry utilized beam currents up to 180 μA with corresponding rates in each of the eight quartz detector bars of almost 0.9 GHz. The quartz bars were read out with PMTs on each end of each bar. The PMTs were fitted with low-gain bases and the current from the bases was integrated. This part of the experiment is referred to as integrating mode.

A number of smaller blocks of time dispersed over the main measurement were devoted to what is referred to below as event mode, which was devoted to measurement of Q^2 and background characterizations. During this portion of the experiment, the beam current was reduced over six orders of magnitude to 50–100 pA, and tracking chambers (horizontal and vertical drift chambers) were inserted into the scattered electron acceptance. Trigger scintillators were also placed in front of the main detector quartz bars. High-gain bases were installed on the quartz bar PMTs to permit counting of individual pulses. The event-mode electronics and DAQ were distinct from those used in integrating mode.

The experiment was also divided into distinct data collection periods. During an initial setup period of several months, various parts of the experiment were debugged. A short commissioning period (early February 2011) took place once all the equipment was finally in place and functioning. Those results are presented in [2]. Following this a period of several months of production running from February to May 2011 (referred to below as Run 1) took place. This was followed by a scheduled 6-month accelerator down period during which some parts of the experiment were opportunistically improved in response to the lessons learned from Run 1. After that a highly efficient period (Run 2) from November 2011 to May 2012 occurred during which most of the data for the primary (integrating mode) measurement were acquired. It is the configuration of the experiment that existed during this final Run 2 period that is described in this paper.

2. Polarized source

Parity-violation experiments have higher demands from the accelerator source than typical experiments performed at JLab, with Q_{weak} being the most demanding to date [20]. In fact, the polarized source is considered part of the experimental apparatus due to the stringent (nanometer scale) requirements placed on HC differences in beam parameters. In addition, the Q_{weak} experiment needed a higher helicity reversal rate and a higher beam current than previous experiments.

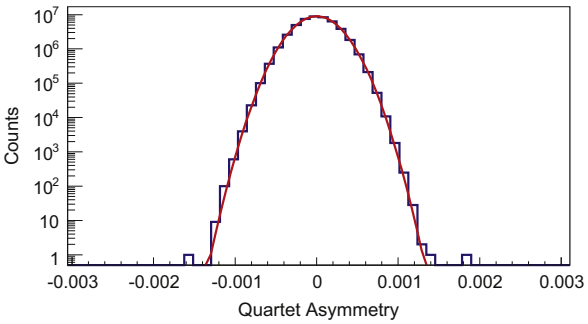

Fig. 3. Measured asymmetry (blinded) of helicity quartets (see text) accumulated over several days. The smooth curve is a Gaussian fit, with an RMS width of 230 ppm.

These requirements led to the development of a new high-voltage switch for the Pockels cell that could provide spin flipping at 960/s [21] and construction of a new higher-bias-voltage photogun [25].

Conceptually, the system is rather simple [26]. Circularly polarized laser light is incident on a photocathode, producing electrons that are accelerated in an electrostatic field. The helicity of the photons is transferred to the electrons. A schematic of the polarized source in the context of the accelerator and experimental hall is shown in Fig. 4.

2.1. Helicity signal

A helicity board located in the injector service building in an electrically isolated VME[20] crate generated five fiber signals: Helicity, nHelicity, Delayed Helicity, Quartet, and Helicity Gate as illustrated in Fig. 4. The Helicity Gates were produced with a frequency of 960.015 Hz, and thus a period of 1041.65 μs. The Helicity signal was used to switch the Pockels cell high voltage. The nHelicity signal (complementary to the Helicity signal) was used to control the helicity magnets. This way the helicity board always drew the same current regardless of the helicity state and further protected against any electrical pickup. In addition, great care was taken within the injector to isolate the reversal signal from cables and ground paths that run throughout the accelerator/endstation complex, as even a weak coupling can result in a significant and varying false asymmetry.

The Delayed Helicity signal was sent to the DAQ and was delayed by eight Helicity Gates, *i.e.*, it reported the state of the electron beam helicity eight Helicity Gates in the past. This technique provides strong protection from electrical pickup that might occur if real-time decoding was used.

The helicity patterns were generated in quartets of four Helicity Gates, where the first and fourth gates had the same helicity, and the second and third had the opposite helicity as the first gate. The helicity of the first gate in each quartet was determined using a 30-bit pseudo-random algorithm. The Quartet signal was true at the beginning of each new pattern, and was also sent to the DAQ.

The Helicity Gate signal sent to the DAQ was defined by the 70 μs period "T_{Settle}" during which the Pockels cell high voltage would change. The remaining 971.65 μs indicated a period of stable helicity "T_{Stable}." The helicity board generated the T_{Settle} signal in the Helicity Gate train 1.0 μs before all other signals. The relative timing of the helicity signals is depicted schematically in Fig. 5.

2.2. Laser and Pockels cell

The laser light was provided by a gain-switched RF[21] pulsed diode operating at 1560 nm, amplified in a fiber amplifier, and then frequency-doubled to 780 nm in a lithium niobate crystal. Three lasers operating at a repetition rate of 499 MHz were used to individually supply beam to each of the three experimental halls at JLab. The beams were combined [26] using a polarizing beam-splitter for the high-current halls and a partially transmissive mirror for the low-intensity hall. A consequence of this arrangement was that the Q_{weak} Hall C beam had opposite polarization to the others.

The linearly polarized laser beams passed through a Pockels cell (an optical element with birefringence dependent on applied voltage) with its fast axis at 45°. At $\sim$2.5 kV, the Pockels cell functioned as a quarter-wave plate and the laser light emerged with circular polarization. Reversing the voltage reversed the birefringence of the crystal and therefore the helicity of the laser beams.

A potentially serious source of systematic error can arise from changes in the beam properties, such as position, angle, and energy that are correlated with the polarization of the beam. Sources of HCBA[22] are dealt with by minimizing the effects as much as possible, and by measuring the beam parameters in the experimental hall and correcting the measured asymmetry for them (Section 3.5).

HCBAs in this experiment were minimized [27] by carefully aligning the optical elements, particularly the Pockels cell. The HC position differences, measured at the first BPM[23] that the electron beam encountered after leaving the photocathode, were the smallest yet measured at JLab ($\leq$20 nm). Illumination of the photocathode using laser beams with a Gaussian spatial profile leads to preferential QE[24] degradation at the center of the laser spot location. After many hours of use, a "QE hole" forms at the photocathode, and the spatial distribution of the electron beam changes accordingly, with more beam produced at the edges of the laser spot, where QE remains high. This gradual evolution of the electron beam spatial distribution causes an increase in measured position differences. The development of a typical QE hole is illustrated in Fig. 6.

The IHWP[25] was the last optical element before the Pockels cell, and its function was to reverse the polarization of the beam without changing the trajectory through the Pockels cell. It was alternately inserted and removed approximately every 8 h. This slow helicity reversal was used to cancel HCBAs related to lensing or steering by the Pockels cell crystal, by forming the difference of asymmetries measured with the IHWP in and out.

The faster Pockels cell high-voltage switch [21] developed for the Q_{weak} experiment was constructed using high-voltage optical diodes [22] that "reverse conduct" when light is applied. The diodes were fast enough to switch the $\sim$2.5 kV required within about 60 μs, by shining light from LEDs[26] on them. This had the additional advantage of providing electrical isolation to prevent leakage of the helicity signal into the electronics. The voltage was ramped up in stages over the transition to minimize induced oscillations, or "ringing." The new switch had much lower capacitance than previous MOSFET[27] switches [23] and virtually eliminated issues that previously resulted from voltage droop. In order to ensure that the transition was complete, 70 μs were allowed to elapse before data-taking was resumed. This represented a 6.72% dead time from helicity reversal at 960/s. Simple schematic diagrams illustrating the difference between the new and old switching schemes are provided in Fig. 7.

Strained-superlattice photocathodes exhibit "QE anisotropy," which is the terminology that describes photoelectron yield that

[20] VERSAModule Eurocard.
[21] Radio frequency.
[22] Helicity-correlated beam asymmetry.
[23] Beam position monitor.
[24] Quantum efficiency.
[25] Insertable half wave plate.
[26] Light emitting diode.
[27] Metal oxide semiconductor field-effect transistor.

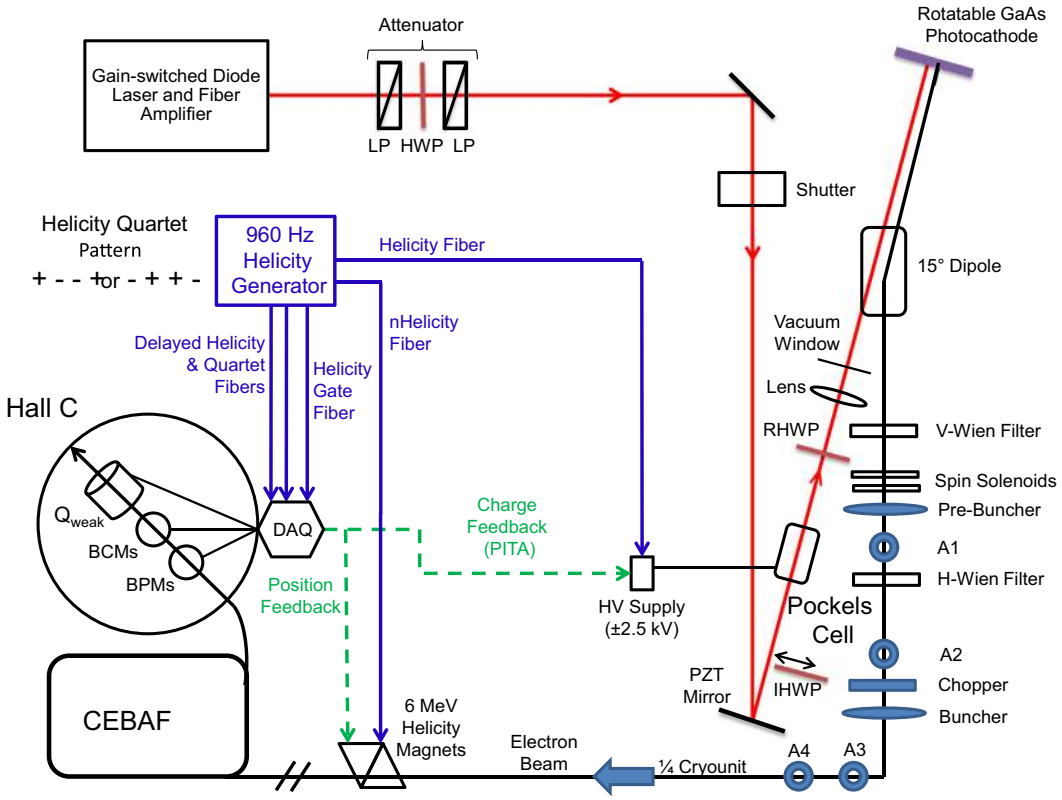

Fig. 4. A schematic of the polarized injector components (see text) used for the Q_{weak} experiment.

varies with the orientation of the incident linearly polarized light. The QE of typical strained-superlattice photocathodes can vary by $\sim 4\%$, depending on the orientation of incident linearly polarized light. Although great lengths were taken to provide 100% circularly polarized light, in practice perfect circular polarization was not achieved. Furthermore the residual linear polarization component varied across the beam spot, giving rise to higher-moment effects such as helicity-correlated position differences. To address this issue, the RHWP[28] was used to rotate the residual linear polarization and provide equal QE for the two helicity states. In practice a small residual sensitivity to asymmetric linear polarization was allowed, so that asymmetric shifts in the Pockels cell voltages could be used to counteract effects from downstream elements. A different orientation of the RHWP was required when the IHWP was inserted. More details on the optimization of the polarized source can be found in [24].

The final element that the laser beam encountered before the vacuum window and the photocathode was a lens which served both to determine the size of the laser spot on the photocathode and, by virtue of a remote motion mechanism, to move the position of the spot on the photocathode. The effect of the vacuum window birefringence on the laser polarization was minimized by rotating the photocathode.

2.3. Photocathode and gun

The photocathode was a p-doped strained-superlattice GaAs/GaAsP wafer which allows spin-selective promotion of electrons to the conduction band by photons with energies slightly larger than the semiconductor band gap. The surface of the photocathode was activated with Cesium and NF_3 to reduce the work function and

[28] Rotatable half wave plate.

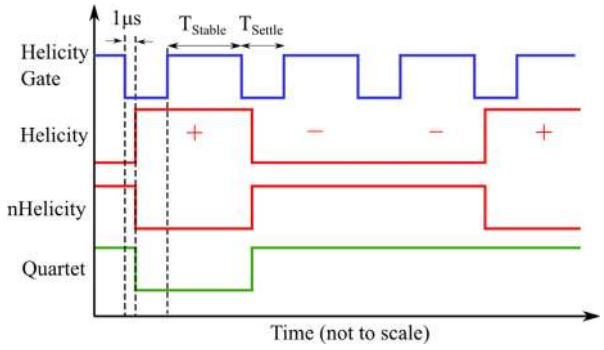

Fig. 5. Timing diagram of the helicity signals from the polarized source. See text for details. The scale of the horizontal axis is exaggerated to show details of the signal timing.

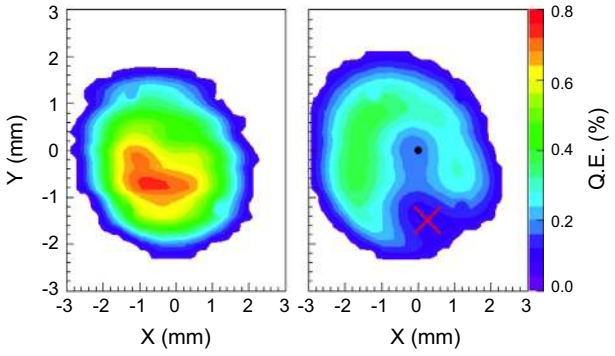

Fig. 6. QE profile scans before (left) and after (right) a four-week period of high current running. In the latter figure, the "dot" shows the electrostatic center and the "X" shows the spot from where 180 μA beam was delivered to the experiment. The active area was ~ 5 mm in diameter and the laser spot size was 1 mm in diameter.

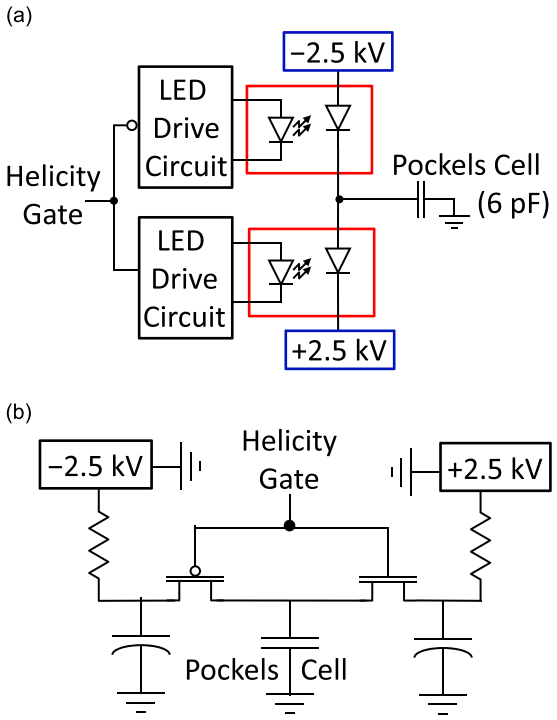

Fig. 7. (a) Fast Pockels cell high-voltage switch developed for the Q_{weak} experiment. The Pockels cell can be viewed as a strictly capacitive device of 6 pf. Because these opto-couplers are so small, they could be mounted directly to the top of the cell. This helped limit the cable capacitance and stray inductance. (b) A diagram of the old Pockels cell HV circuit, which incorporated fast HV transistor switches.

obtain the negative electron affinity required to extract an electron beam. During Q_{weak}, the photocathode was "reactivated" once during Run 1, and once during Run 2. As mentioned above, the photocathode exhibited a QE anisotropy of 4%. This PITA[29] was responsible for most of the HCBAs, particularly as there were analyzing gradients in the photocathode and polarization gradients in the beam. The PITA effect was used for charge feedback. Small changes to the Pockels cell voltage for each helicity state were used to change the amount of linear light in the laser beam such that, once analyzed by the photocathode, the number of electrons was the same in each state.

A new "inverted electron gun" [25] was developed for the Q_{weak} experiment. This design utilized a compact, tapered ceramic insulator that extended into the vacuum chamber which increased the distance between biased and grounded parts of the gun and reduced the amount of metal biased at high voltage. Electrons leaving the photocathode experienced a field strength of $\sim$2 MV/m and the field strength within the cathode/anode gap was $\sim$5 MV/m. Although the maximum field strength inside the gun was $\sim$9 MV/m, the gun operated reliably at 130 kV without measurable field emission. The experiment ran consistently at beam currents of $\sim$180 μA, significantly higher than has been delivered previously at JLab. Space-charge induced emittance growth at this current is significant, and beam loss at the injector apertures A1–A4 (see Fig. 4) would have been difficult to eliminate using the previous photogun [21] operating at 100 kV. Beam loss during Q_{weak} was typically 3% or less, while operating an injector bunching cavity at relatively modest field strength.

During Run 1 only modest $1/e$ photocathode charge-lifetimes of $\sim$50 C per laser spot were achieved. Several different spots could be utilized before the photocathode required a reactivation

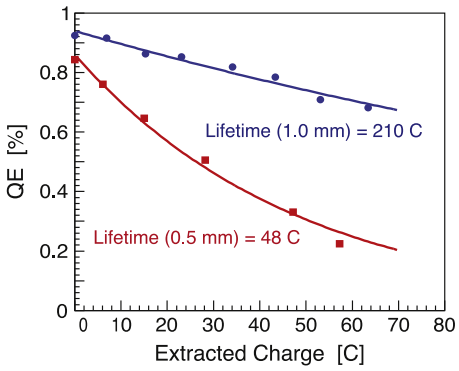

Fig. 8. The measured QE is plotted against the charge extracted from the photocathode. The fitted curves represent $1/e$ charge-lifetimes of a spot on the photocathode, before (square points) and after (circles) the spot size was increased by changing to a lens with a longer focal length.

cycle. Ion back-bombardment is the predominant mechanism degrading the photocathode QE during electron emission [26]. This effect was mitigated by replacing the 1.5 m focal length lens with one of 2.0 m, thus increasing the FWHM[30] of the laser spot from 0.5 mm to 1.0 mm and distributing the ion damage over a bigger region [28]. Cathode lifetimes of $\sim$200 C were achieved during Run 2 with the larger laser spot. Fig. 8 shows $1/e$ fits to the daily-measured QE against the extracted beam charge obtained in both configurations.

2.4. Injector

The purpose of the injector section is to accelerate the beam to relativistic velocities synchronized with the CEBAF[31] linacs. For a high-current beam, longitudinal bunching is also required.

The apertures and the chopper [29] were used to limit the emittance of the beam by trimming the transverse and temporal (longitudinal) dimensions, respectively. Halfway between the photocathode and the chopper (in the 130 keV region), the pre-buncher prepared the longitudinal component of the beam for the chopper. The chopper was a pair of 499 MHz RF deflecting cavities phased to sweep the beam in a circle with a revolution frequency of 499 MHz. The chopper aperture was kept open at its widest extent, approximately 20°, throughout the experiment. Losses could be significant in these areas since the space-charge of the high-current beam caused the beam to expand in all dimensions. In practice, a significant increase in the width of the charge asymmetry distribution measured by the experiment indicated when the beam trajectory in the injector needed to be tuned to minimize interception.

The two-Wien spin flipper was composed of a vertical Wien filter followed by two solenoids and then a horizontal Wien, described in detail in Ref. [30]. Ideally the system reverses the polarization of the electron beam in the injector without changing the optical focusing properties of the system, by reversing the current in both solenoids. This reverses the correlation between the helicity of the laser and photo-produced electrons, and the electrons that ultimately arrive in the experimental hall. This canceled polarization induced HCBAs, most notably those related to differences in the beam spot size, which, unlike the trajectory, were not directly measured in the experiment. The two-Wien system was changed monthly throughout the experiment.

The helicity magnets were a set of four air-core dipole magnets placed in the 6 MeV region of the injector beamline to kick the beam differentially for each helicity state. They were used to

[29] Polarization induced transport asymmetry.

[30] Full width at half maximum.

[31] Continuous electron beam accelerator facility.

control the HC position (X, Y) and, less effectively, angle (X', Y') differences. Sensitivities were determined periodically and corrections were applied approximately daily to reduce the differences.

There were two RF cavities in the injector used for velocity bunching the beam: the buncher and the pre-buncher (see Fig. 4). They were run with a phase offset so that the beam pulse would arrive at the zero-crossing potential and feel an accelerating force at the back of the bunch and a decelerating force at the front of the bunch. Despite using these cavities, there were still issues related to beam blowup from the large space charge, such as large-halo scraping on apertures in the experimental hall. In order to deal with this during Run 2, the injector was given a special ("M56") tune in order to further bunch the beam. The injector chicane was tuned to give a standard magnetic compression for a relativistic beam, equivalent in effect to velocity bunching at low energy. The quadrupole magnets in the chicane were set to give the lower-energy electrons, which were also towards the back of the bunch, a shorter path through the chicane, allowing them to catch up. This procedure resulted in a factor of 2 reduction in bunch length arriving at the accelerator.

3. Beam transport and diagnostics

3.1. Accelerator

At the time of the Q_{weak} experiment, the CEBAF accelerator [19] consisted of a single-pass 62 MeV injector (see Section 2.4), and two 548 MeV superconducting linacs joined by recirculating arcs allowing one to five pass beam. The two linacs are typically operated at equal energy, with the injector at 11.25% of the North Linac energy. Except for a brief period of 2-pass, 1.16 GeV operation at the start of Run 2, the experiment used 1-pass beam of 1.16 GeV. The 2-pass running provided a useful check for the experiment as an independent $(g-2)$ helicity reversal relative to 1-pass operation.

A resistive copper cavity accelerated the beam leaving the polarized source from 130 keV to 500 keV. A pair of RF superconducting cavities accelerated the beam from 500 keV to 6 MeV, and contain an RF skew quadrupole term which couples the x and y beta functions. The excellent normalized emittance provided by the photogun is therefore degraded, typically by an order of magnitude.

After acceleration from 6 MeV to 62 MeV the beam passed through a region used to match the transverse optics to the North Linac. This match generally preserves normalized emittance. After the matching region a chicane is used to avoid recirculated beams of higher energy. The dispersion in the chicane allowed for injector energy feedback. The injector and higher-energy beams were rendered co-linear in a dipole at the start of the North Linac. The beam for Q_{weak} then went through the North Linac, was separated vertically from other energy beams, went through a 180° arc, was merged with other energy beams from the other arcs, and passed into the South Linac. It was extracted from among the other beams by a 499 MHz RF separator and a series of septum magnets. The beam was then directed into the Hall C arc, consisting of (quads and) eight 3 m long dipole magnets which deflected the beam 34.3° to experimental Hall C. A transverse optics matching region before the Hall C arc was used to restore the desired beam envelope functions to design.

A fast feedback system minimized excursions in both planes at the entrance and exit of the Hall C arc and at the high-dispersion BCM.[32] Four air-core correctors and the last RF zone in the South Linac were the actuators for this feedback system with ~ 1 kHz response.

[32] Beam charge monitor.

A second optics adjustment region between the Hall C arc and the Compton polarimeter prepared the beam waist needed for polarimetry. After the Compton polarimeter there was a final array of quadrupoles to match the beam to the LH_2 target and finally a set of raster magnets to diffuse the ~ 200 μm beam profile at the cryotarget to (typically) 4×4 mm^2.

The raster reduced the effects of target boiling (see Section 5.3) and prevented the beam from burning through the target windows. The beam spot on the target traced a uniform, square Lissajous pattern generated by two air-core magnets driven by triangular waves with fundamental frequencies of $\nu_1 = 24.960$ and $\nu_2 = 25.920$ kHz. The raster pattern repeated with a frequency of $(\nu_2 - \nu_1) = 960.000$ Hz, so each of the 960.015/s Helicity Gates integrated over a nearly complete raster pattern. If the raster period was substantially longer than the Helicity Gate period, then each helicity event would integrate over a different portion of the target face and introduce additional noise in the detector asymmetries. This was verified in a set of test runs with 160 μA beam current. The asymmetry width measured for the 960 Hz raster patterns was 239 ppm, and increased for raster patterns at 480 Hz (240 ppm), and 240 Hz (253 ppm).

At the exit of the experimental hall, the transition to the beam-dump tunnel was redesigned to withstand the greater power density of the beam used in the experiment. The window separating the upstream beamline vacuum from the helium-filled downstream beamline to the beam dump consisted of two hemispherical ($r = 38$ cm) aluminum 2024-T6 windows (0.76 mm thick upstream, 0.51 mm thick downstream) separated by 2.3 cm of water circulated through a chiller.

3.2. Beam current measurement

The Q_{weak} experiment employed six RF cavity BCMs. They were located upstream of the target at distances of 16 m (BCM5, BCM7 and 8), 13.4 m (BCM1 and 2), and 2.7 m (BCM6). Calibrations of the BCMs between 1 and 180 μA were performed using a Parametric Current Transformer [31] (Bergoz Unser monitor) in the Hall C beamline. After calibration, the BCM linearity was observed to be better than 0.5% between 20 and 180 μA. At the extremely low beam currents used for the event mode of the experiment (10 nA–1 μA), a Faraday cup in the injector was used for calibration.

The BCMs provided stable, low noise, continuous (non-invasive) beam current measurements. To avoid radiation damage, the sensitive BCM electronics were located outside the experimental hall. BCM1, BCM2, and the Unser used analog receivers. Digital receivers developed for the Q_{weak} experiment were used with four additional new BCMs. The BCM cavities were tuned to the third harmonic of the beam frequency (1497 MHz), and temperature stabilized at 43 °C to preserve the tune. The analog receivers frequency downconverted the cavity outputs to 1 MHz, and then used RMS[33]-to-DC converters to demodulate the signals. The digital receivers downconverted to 45 MHz, and then digitally sampled and processed the signals. In both cases, voltage levels proportional to beam current and band-limited to ~ 100 kHz were provided to the 18-bit sampling ADCs[34] [32] described in Section 10.2.

Two metrics were used to assess the performance of the BCMs. The most useful was the width of the DD[35] of asymmetries derived from a pair of BCMs, because fluctuations in the beam charge canceled, resulting in a metric sensitive only to the instrumental resolution of a BCM pair. For example, the DD of BCMs 7 and 8 is

$$DD_{78} = \frac{Q_7^+ - Q_7^-}{Q_7^+ + Q_7^-} - \frac{Q_8^+ - Q_8^-}{Q_8^+ + Q_8^-} \tag{5}$$

[33] Root-mean-square.
[34] Analog to digital converter.
[35] Double difference.

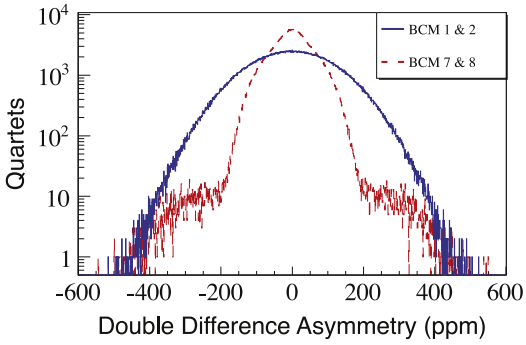

Fig. 9. Charge asymmetry double difference plots for two pairs of BCMs from a typical 1 h run. The DD_{12} (broad curve) has an RMS width of 115 ppm. The DD_{78} (skinny curve with shoulders) has an RMS width of only 57 ppm.

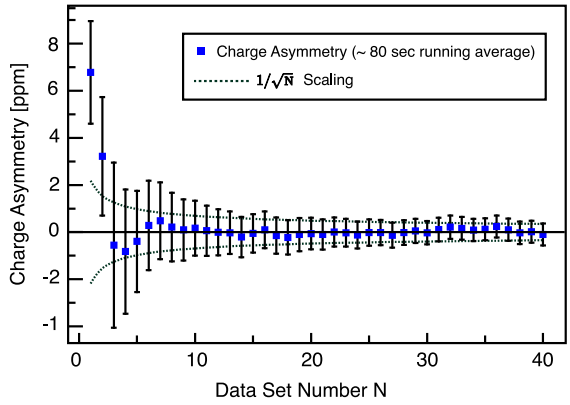

Fig. 10. Running charge asymmetry from a typical 1 h run showing the effect of charge feedback applied over 80 s intervals [34]. The horizontal axis shows the number of 80 s intervals. The dotted curve is the $1/\sqrt{N}$ statistical convergence.

where Q_i^j denotes the charge measured by BCM i for beam helicity j. The resolution of an individual BCM was taken as its $DD/\sqrt{2}$. The other BCM performance metric was the width of the main detector asymmetry as defined in Eq. (2) and discussed in Section 1.3. However, the BCM resolution was only one of the several effects contributing in quadrature to that width.

During Run 1 the experiment relied primarily on BCM1 and 2, which provided a DD_{12} of 100–140 ppm (see Fig. 9). BCM5 and 6 were connected to prototype digital receivers that were located in the experimental hall and sustained radiation damage. Between Run 1 and 2, BCM7 and 8 were added and the new digital receivers for BCMs 5–8 were installed outside the hall. The new electronics took advantage of improved digital signal processing techniques and utilized 18-bit, 1 MHz DACs[36] to generate the output voltage. Finally, air-core coaxial cables were replaced with Heliax [33] cables. The resulting DD_{78} was typically only $\sim$60 ppm, so BCM8 was used for charge normalization in Run 2.

Assuming a detector non-linearity of 1%, the experiment required that the overall helicity-correlated IA[37] be kept below 100 ppb in order to limit this contribution to the uncertainty in the asymmetry measurement to <1 ppb. Since the measured IA was typically a few ppm over a 1 min interval, an active charge feedback system was used. The cumulative IA was measured in 80 s intervals (see Fig. 10), and the feedback scheme adjusted the Pockels cell voltages (PITA offsets) at the polarized source (see Section 2.3) to null it. Over a typical month of running, the IA was typically only 40 ppb [34].

3.3. Beam position and angle

Continuous beam position monitoring in the experiment was carried out using stripline monitors [35,36] equipped with two $+/-$ pairs of perpendicular antennas tuned to the RF structure of the beam. The readout of each $+/-$ pair was multiplexed using switched-electrode electronics every 4.2 μs to eliminate the effects of gain differences in the electronics. Each of the four antennas from each BPM was read out for each helicity state of the beam into 18-bit sampling ADCs custom-built [32] for this experiment's faster reversal rate, described in Section 10.2. There were 24 BPMs read out in the injector beamline, and 23 in the Hall C beamline. The BPMs were used with beam currents between 50 nA and 180 μA.

The beam position and the angle at the LH_2 target were determined [37] from a linear least squares fit of 4 or 5 BPMs in a magnetic field-free drift region between 1.5 m and 10.5 m upstream of the target. Using two BPMs as a reference, the offsets of the remaining BPMs in front of the target were adjusted by $\sim$1 mm to bring them into agreement. These offsets were stable over the 2 years of the experiment at the 25 μm level. Typical position resolutions of 1 μm (1.7 μm) were achieved with five (4) BPMs using methods similar to the DD technique described in Section 3.2, implying $\sim$1 nm scale resolution in an hour. Likewise, angle resolution at the target was typically 150 nrad.

A slow (1 s update) position lock was implemented to maintain the desired beam position and angle on the target, using this calculated target position in conjunction with pairs of corrector magnets upstream of the BPMs.

3.4. Beam energy

Two types of beam-energy measurements were required for the experiment: an absolute beam-energy measurement for the incident energy and Q^2 determination, and the energy-asymmetry measurement at the target to remove false asymmetries generated by HC energy fluctuations.

Position sensitive 3-wire scanners (harps [38]) located before, in the middle, and after the Hall C arc were used for invasive and therefore infrequent energy measurements accurate to $\sim 10^{-3}$. These were carried out by utilizing the Hall C arc beamline as a spectrometer [39] according to

$$p(\mathrm{GeV/c}) = \frac{0.3}{\sin\Theta}\int B(\mathrm{T})\, dl(\mathrm{m}) \tag{6}$$

where Θ is the angle (34.3°) by which the electron beam bends in the arc and $\int B\, dl$ is the magnetic field integral over the eight 3 m long dipoles in the arc beamline [40]. With the arc quadrupole and corrector magnets off during these energy measurements, the momentum dispersion is 12 cm/% at the end of the arc. These invasive energy measurements were used to benchmark continuous (non-invasive) energy measurements with a relative accuracy of $\sim$100 ppm obtained using BPMs along the Hall C beamline in conjunction with knowledge of the arc optics and dipole magnetic fields.

The HC beam-energy asymmetry at the target was determined using the BPM (BPM3C12) located in the region of highest dispersion (typically 4 cm/%) in the Hall C arc. The horizontal (X) beam-position differences measured at BPM3C12 are sensitive to position, angle, and energy differences. Therefore, relative energy differences

[36] Digital to analog converter.
[37] Charge asymmetry.

at the target were obtained from

$$\frac{\Delta P}{P}=\frac{\Delta X_{3C12}}{411}-\frac{\Delta X_{\text{target}}}{596}+\frac{\Delta X'_{\text{target}}}{0.443} \quad (7)$$

where the subscripts indicate the beam position differences (in cm) at 3C12/target, X'_{target} represents the (horizontal) beam angle in X at the target (in radians) and the denominators on the right of Eq. (7) account for the first-order transport matrix elements for beam propagation between 3C12 and the target.

3.5. Beam modulation

As described above in Eq. (3) and Section 2.2, unwanted HC changes in the transverse beam positions X (horizontal) and Y (vertical), beam angles X' and Y', and incident energy E on the target give rise to false asymmetries (HCBA). These HCBAs $A_{\text{beam}}(E, X, Y, X', Y')$ can be heavily suppressed with careful tuning at the polarized source and a symmetric detector array. However, the residual effects must be measured and controlled. A_{beam} is determined using the following expression:

$$A_{\text{beam}}=\sum_{i=1,5}\frac{\partial A}{\partial \chi_i}\Delta\chi_i. \quad (8)$$

Here the slopes $\partial A/\partial\chi_i$ are the measured detector sensitivities of the asymmetry A_{raw} (defined in Eq. (2)) to changes in the beam parameters χ_i at the helicity quartet level, and $\Delta\chi_i$ is the HC difference of each beam parameter χ_i measured at the quartet level. The five BPMs described in Section 3.3 were used to continuously measure the HC beam position and angle differences at the target. The measurement of the HC energy difference relied on BPM3C12, as described in Eq. (7) of Section 3.4.

The natural jitter of the beam can be, and was used to determine the detector sensitivities $\partial A/\partial\chi_i$. However, better decoupling of the five sensitivities was achieved by varying the beam parameters in a controlled manner using a beam modulation system built specifically for this purpose. Decoupled position and angle motions were separately produced by varying the current in pairs of air-core magnets placed along the beamline; two pairs in X and two pairs in Y approximately 82 and 93 m upstream of the target. Optics simulations [41] were used to determine the optimum placement of the coil pairs along the beamline which produced the offsets in position and angle desired at the target. Changes in energy were produced by varying the power input to a cavity in the accelerator's South Linac, and monitored using the response of BPM3C12 at the point of highest dispersion in the Hall C arc. The beam was driven at ~ 125 Hz with the modulation system for 20 s every 320 s for the duration of the experiment.

Typical beam modulation amplitudes at the target, as well as typical monthly results measured for the HC beam properties $\Delta\chi_i$ and detector sensitivities $\partial A/\partial\chi_i$ can be found in Table 2. The HCBAs for X and X' are anti-correlated and largely cancel. The same is true for Y and Y'. The uncertainties associated with the monthly HC position (angle) differences $\Delta\chi_i$ are 0.07 nm (0.01 nrad) based on the quartet level BPM resolution discussed in Section 3.3 of 1 μm (0.2 μrad) over the 2×10^8 quartets in the monthly period shown in Table 2.

3.6. Beam halo monitors

Several PMT monitors straddled the beamline between 1 m and 5 m upstream of the LH_2 target to monitor beam halo, providing crucial feedback used to tune the beam. Four monitors had lucite blocks coupled to their 5.1 cm diameter PMTs, and two used small scintillator blocks. All six monitors used 12-stage Photonis XP2262B PMTs read out in event (pulse-counting) mode. Each halo monitor pair was shielded with lead and pointed upstream at a retractable halo "target" 6 m upstream of the LH_2 target. The halo target consisted of a 2.8 cm $\times$ 5.1 cm aluminum frame 1 mm thick with a 13 mm diameter circular hole and an 8 mm $\times$ 8 mm square hole cut out of it. The target could be positioned with a linear actuator such that either hole (or the frame) could be positioned in the beam, or it could be retracted completely out of the beam pipe.

An absolute measure of the beam halo was obtained by calibrating the halo monitors with beam passing through the 1 mm thick halo frame. The most useful monitors for absolute determination of the beam halo fraction were two of the lucite monitors (one with a 2 cm thick lead block in front to suppress low-energy particles). These were well shielded on five sides with lead, and located 16.5 cm from the beam centerline on opposite sides of the beampipe 75 cm downstream of the halo target. The mean scattering angle of these monitors relative to the halo target was $\sim 12.4^\circ$. Background from upstream of the halo target was accounted for with the halo target out. With this correction, the absolute halo fraction was determined to a precision of $\sim 2\times10^{-8}$ at a beam current of 180 μA. In addition to these dedicated measurements of the halo fraction, the 13 mm hole was in place about half the time during the experiment to provide a continuous monitor of the beam halo. Typical measured beam halo was between 0.1 and 1 ppm.

Table 2
Typical amplitudes used for driven beam modulation (column 2). Columns 3 and 4 provide typical average monthly results measured during Run 2 for the HC beam parameter differences $\Delta\chi_i$ and detector sensitivities $\partial A/\partial\chi_i$ for the beam parameters i listed in the first column. The total HCBA for this example is only 0.4 ppb. The uncertainties associated with $\Delta\chi_i$ and $\partial A/\partial\chi_i$ are discussed in the text.

Beam parameter	Modulation amplitude	Msrd $\Delta\chi_i$ (monthly)	Msrd $\partial A/\partial\chi_i$ (monthly)
X	± 125 μm	−3.3 nm	−2.11 ppm/μm
Y	± 125 μm	2.5 nm	0.24 ppm/μm
X'	± 5 μrad	−0.7 nrad	100.2 ppm/μrad
Y'	± 5 μrad	0.02 nrad	−0.0 ppm/μrad
Energy	± 61 ppm, (~70 keV)	0.1 nm	−1.56 ppm/μm

4. Beam polarization

Measurement of the beam polarization was expected to be the largest systematic uncertainty in the experiment. An existing Møller polarimeter has routinely provided precise beam polarization measurements at $\lesssim 1.5\%$ in Hall C for many years. However, these measurements can only be performed at beam currents much lower than those employed in the experiment (typically $\lesssim$2 μA, although beam currents up to 20 μA have been employed). The measurements are invasive, and therefore performed infrequently.

Therefore, the Møller polarimeter was augmented with a new, non-invasive Compton polarimeter which provided continuous polarization measurements at the full 180 μA of the Q_{weak} experiment. A statistical precision better than 1% per hour was achieved. The absolute polarization determined independently from the two polarimeters was cross-checked (once) with Compton polarimeter measurements at 4.5 μA bracketed with Møller polarimeter measurements at the same beam current.

4.1. The Møller polarimeter

The beam polarization was measured using the existing Hall C Møller polarimeter [42] 2–3 times per week. Extensive studies were done for this experiment to characterize the uncertainties and ensure sub-percent precision.

The Møller polarimeter measured the parity-conserving $\vec{e}\,\vec{e}$ cross-section asymmetry A_{zz}, for which the analyzing power is

precisely known. The Hall C Møller used a split superconducting solenoid to brute-force polarize a 1 μm thick pure iron target foil along the beam direction. The 3.5 T solenoid field was sufficiently above the 2.2 T saturation point of iron to fully saturate the foil. Since only the valence electrons contribute to the magnetization, the total target polarization was only about 8% averaged over all the electrons in the atom. Scattered and recoil electrons were detected in coincidence using a near-symmetric apparatus, with one electron detector aperture slightly smaller than the other to cleanly define the acceptance. The use of a narrow timing window minimized accidentals and reduced the signal from Mott scattering from the iron nucleus, the dominant background [43]. Fig. 11 shows a schematic of the device.

Table 3 summarizes the uncertainties. The largest comes from scattering off the unpolarized inner electron shells (the Levchuk effect) [44]. Since the Møller measurements were invasive and limited to low current ($\sim 2\,\mu A$), a conservative uncertainty was included to account for potential effects due to extrapolation to the higher beam current used in the experiment. This concern was also addressed by comparison with the results of the Compton polarimeter discussed in Section 4.2.

During Run 1, an intermittent short in one of the coils of quadrupole 3 (see Fig. 11) affected the acceptance and therefore the analyzing power of the polarimeter at the few-percent level. To account for this, the Møller simulation used to provide the polarimeter acceptance was modified to include a correspondingly altered quadrupole field map using a POISSON magneto-static field generator [45]. Hall probes in the quad were used to compare to simulations of the polarimeter response with and without the short. An uncertainty of 0.89% was added to the Run 1 commissioning Møller polarization measurements [2] to account for this effect, which was absent in Run 2.

4.2. The Compton polarimeter

A layout of the Compton polarimeter based on $\vec{\gamma}\,\vec{e} \longrightarrow \gamma e$ which was built for the experiment is shown in Fig. 12. The electron beam was deflected vertically by two dipole magnets to where it could interact with photons in a moderate-gain laser cavity. The unscattered electron beam was deflected back to the nominal beamline with a second pair of dipole magnets. The third of the four chicane magnets also served to spatially separate electrons that had undergone Compton scattering from the rest of the beam. These Compton recoil electrons were detected in a multi-plane diamond strip detector. Compton scattered photons passed through the third magnet and were detected in an array of $PbWO_4$ crystals. The absolute beam polarization was continuously measured to an accuracy of better than 1% per hour with the Compton electron detector.

4.2.1. Compton laser system

The photon target for the Compton electron beam polarimeter was composed of a Coherent Verdi 10 laser [46] with an output of 10 W at 532 nm and locked to an external Fabry–Perot optical cavity with a gain of approximately 200. The optical

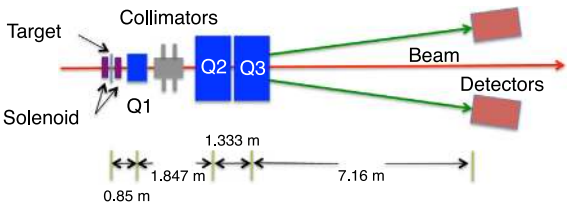

Fig. 11. The Hall C Møller polarimeter. Only quadrupole magnets 1 and 3 were used during Q_{weak}; quadrupole 2 was installed in preparation for the JLab 12 GeV program.

Table 3
The systematic uncertainties of the Hall C Møller polarimeter for Run 2 of the experiment. An additional uncertainty was present during Run 1 due to an intermittent short in one of the quadrupoles of the polarimeter (see text).

Source	Uncertainty	dA/A (%)
Beam position X	0.5 mm	0.17
Beam position Y	0.5 mm	0.28
Beam direction X'	0.5 mrad	0.1
Beam direction Y'	0.5 mrad	0.1
Q1 current	2%	0.07
Q3 current	3%	0.05
Q3 position	1 mm	0.01
Multiple scattering	10%	0.01
Levchuk effect	10%	0.33
Collimator position	0.5 mm	0.03
Target temperature	100%	0.14
B-field direction	2°	0.14
B-field strength	5%	0.03
Spin depolarization	–	0.25
Electronic dead time	100%	0.05
Solenoid focusing	100%	0.21
Solenoid position (X, Y)	0.5 mm	0.23
High current extrap.	–	0.5
Monte Carlo statistics	–	0.14
	Total	0.83

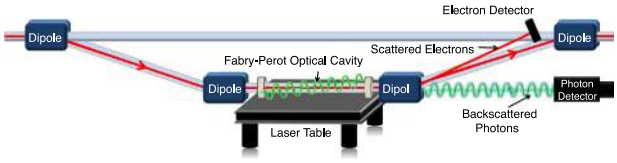

Fig. 12. A sketch showing the layout of the Compton polarimeter. The total length of the dipole chicane was 11.1 m, and the laser interaction region was 57 cm below the undeflected beamline. The electron beam trajectory is from left to right in the figure.

elements used to produce the photon target were located on an optics table 57 cm below the electron beam. The ~ 80 cm long optical cavity crossed the electron beam at 1.3°.

A variety of optics were utilized on the optics table to control the shape, intensity, helicity, and polarization of the laser. The 100% linearly polarized laser beam was changed to 99.9% circular polarization in the cavity by means of a linear polarizer and a quarter-wave plate. The laser polarization was continuously measured to $\pm 0.2\%$ using reflected light at the entrance mirror of the optical cavity [47,48].

The optical cavity was locked using the Pound–Drever–Hall locking technique [49] feeding back on the laser wavelength via PZT[38]-actuated mirrors, internal to the Verdi laser cavity. The laser frequency was modulated using an electro-optical modulator. The modulation signal, when mixed with the signal from a photodiode monitoring the reflected light from the Fabry–Perot cavity, provided an error signal. The error signal was fed into a PID[39] feedback circuit which maintained the optical cavity lock by appropriately adjusting the laser wavelength via the internal PZT actuators.

The transmitted beam was split into multiple beams using a holographic beam sampler to simultaneously monitor its polarization, power, position, and image.

4.2.2. Compton photon detector

Photons which were Compton back-scattered from the electron beam passed straight through the third dipole of the chicane and

[38] Piezoelectric transducer.
[39] Proportional-integral-differential.

entered a calorimeter array composed of four 20 cm long stacked $PbWO_4$ crystals each with a cross-section of 3×3 cm^2. A single 7.6 cm diameter Hamamatsu R4885 [50] PMT with a gain of 5×10^6 was attached with optical grease to the back face of the calorimeter. Both were inside a thermally isolated box cooled to ~ 14 °C which increased the light yield of the crystals by $\sim 20\%$ compared to room temperature. The photon signals were digitized with a 12-bit, 4 V range, flash ADC (Struck SIS3320 [51]) sampling at 250 MHz. An energy-weighted integral over all photon energies was performed and read out at the helicity flip rate of 960/s. During each helicity period, at least one set of 256 contiguous samples was read out to monitor the health and help determine the linearity of the detector. The linearity was studied with a system modeled after [52], composed of two LEDs pulsing for ~ 60 ns with one LED serving as a reference signal and the other LED with intensity spanning the response range of the detector.

Due to the challenging nature of the linearity measurements, absolute polarizations have not been extracted from the Run 2 photon detector data as of this writing. The analysis is currently focusing on relative comparisons with the electron detector results. The quasi-independent absolute beam polarization measurements provided by the electron detector are discussed next.

4.2.3. Compton electron detector

The recoil electrons from the Compton scattering process were momentum analyzed in the third dipole magnet and detected by a set of micro-strip detectors located just upstream of the fourth dipole magnet. The micro-strip electron detectors were made from $21 \times 21 \times 0.5$ mm^3 plates of chemical vapor deposited diamond [53]. Each diamond plate had 96 metalized horizontal strips with a pitch of 200 μm (including a 20 μm gap) on one side (front) and a single metalized electrode 100 μm [54] thick covering the entire diamond surface on the opposite side. Each diamond plate was epoxied to a 60 mm $\times$ 80 mm alumina substrate. Each of the 96 strips was wire bonded to gold traces on the alumina substrate which terminated on two 50-pin high-density connectors [55] placed on either side of the detector plate.

The four detector planes were spaced ~ 1 cm apart and inclined 10.2° to align them perpendicular to the electron beam exiting the third dipole in the chicane. The detector stack was attached to a vertical linear feedthrough with 30.5 cm of travel inside a vacuum can. Under normal operating conditions the detectors were lowered to a vertical distance of ~ 7 mm from the main electron beam. When not in use the detectors were retracted into a section of the vacuum chamber well separated from the electron beam. At the bias voltage of -400 V maintained across each plane, the raw charge signal was ~ 9000 e$^-$ per hit. Custom-built low-noise QWADs[40] [32] were used with a typical gain of 100 mV/fC.

The digital signals from the QWADs were carried via 60 m of cable to four FPGA[41] based general purpose logic boards [56]. These provided the trigger and reconditioned the signals for the independent Compton data acquisition system [57].

The data were collected in ~ 1 hr long runs which were later decoded and used to fill histograms of hits on each detector strip for each electron beam helicity. Laser-off data were used to build background spectra. Only 3 out of the 4 detector planes were operational during the experiment. A typical strip hit spectrum is shown in Fig. 13. Using the background corrected strip hit spectra for each electron helicity state, the asymmetry can be determined as a function of electron momentum. These asymmetry spectra were compared with a QED[42] calculation [58] to obtain the electron beam

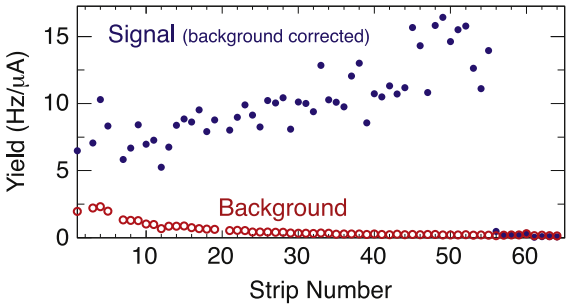

Fig. 13. A spectrum of normalized yield for each strip of a single detector plane. The three empty strips correspond to strips that were too noisy and had to be masked. Strip 1 is closest (7 mm) to the beam; the Compton edge is at strip 56.

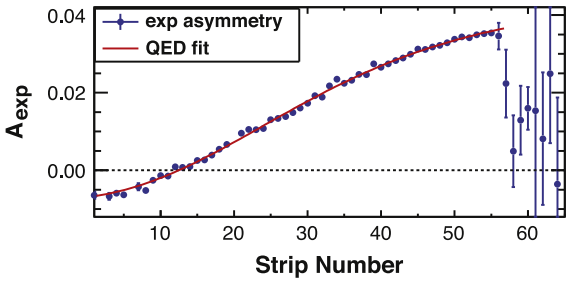

Fig. 14. A spectrum of the measured asymmetry for each strip along with the fit to a QED calculation shown by the solid line. The three missing strips, out of the >50 active strips, have a negligible impact on the quality of the fit and the extracted electron polarization.

polarization. A typical asymmetry spectrum along with the QED calculation is shown in Fig. 14. The electron beam polarization was continuously monitored throughout the Q_{weak} experiment using the Compton polarimeter electron detectors described in this section. The beam polarization obtained using the electron detector was consistent with the Møller polarimeter measurements performed at low beam currents.

Table 4 summarizes the systematic uncertainties associated with the Compton polarimeter. The largest two uncertainties arose from a timing issue which resulted in occasional loss of information from a plane. The effect depended on rate. The preliminary correction for this effect contributed an average of 0.7% to the overall polarization uncertainty, with an additional 0.35% point-to-point variation observed over the course of the experiment.

4.3. Performance

The beam polarization was monitored by both the Møller and Compton polarimeters during the Q_{weak} experiment. In general the Compton polarimeter ran continuously and concurrently with data-taking for the experiment, achieving statistical errors ranging from a little more than 1% per 1-h run (during the latter half of Run 1) to less than 0.5% per 1-h run (Run 2). Each invasive Møller measurement took 4–6 h, and therefore, as previously stated, was used only 2–3 times per week.

During Run 2, both the Møller and Compton polarimeters were functioning correctly and with good efficiency. Results from both devices contributed to the extracted values of the beam polarization for that period. Fig. 15 compares results from both polarimeters where polarization measurements taken under similar beam conditions are plotted. The overall agreement is good. The stability of the beam polarization measured by the Compton polarimeter justifies the time interval chosen for the more infrequent Møller polarimeter measurements. However, Møller measurements were always made immediately before and after changes in the polarized source that

[40] Q_{weak} amplifier-discriminators.
[41] Field programmable gate array.
[42] Quantum electrodynamics.

Table 4
The Hall C Compton polarimeter systematic uncertainties determined for Run 2 of the experiment. The last two rows in the table are preliminary estimates, and are expected to be smaller upon completion of their analysis.

Source	Uncertainty	$\Delta P/P$ (%)
Laser polarization	0.18%	0.18
3rd Dipole field	0.0011 T	0.13
Beam energy	1 MeV	0.08
Detector Z position	1 mm	0.03
Trigger multiplicity	1–3 plane	0.19
Trigger clustering	1–8 strips	0.01
Detector tilt (X)	1°	0.03
Detector tilt (Y)	1°	0.02
Detector tilt (Z)	1°	0.04
Strip eff. variation	0.0–100%	0.1
Detector noise	$\lesssim$20% of rate	0.1
Fringe field	100%	0.05
Radiative corrections	20%	0.05
DAQ ineff. correction	100% (prelim)	0.7
DAQ ineff. pt-to-pt	(prelim)	0.35
Total		0.85

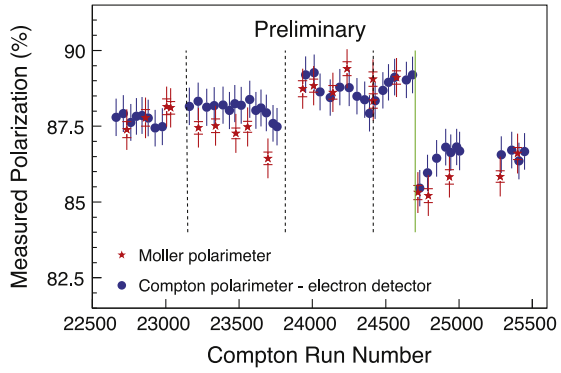

Fig. 15. Beam polarization measurements for the second Q_{weak} run period plotted vs. Compton polarimeter run number (spanning a roughly 6-month period). The solid stars show the Møller measurements with statistical uncertainties (inner) and statistical + point-to-point systematic uncertainties added in quadrature (outer) (see Section 4.1) – the overall normalization uncertainty of 0.64% is not shown. The solid circles show the preliminary results from the Compton polarimeter electron detector – each point represents an average over about 30 h of data. The uncertainties shown represent statistical and estimated systematic errors added in quadrature. Vertical dashed lines denote changes in the position of the electron source laser position on the photocathode, while the solid vertical line marks a heating and subsequent re-activation of the photocathode.

were known to affect the beam polarization: notably laser spot changes or reactivation of the injector photocathode.

The commissioning of the Compton polarimeter was completed near the middle of Run 1, so polarization results for the first part of Run 1 come exclusively from the Møller polarimeter. The quad problem noted earlier in Section 4.1 significantly complicated the analysis of Møller data from that period and resulted in greater uncertainty for the affected Run 1 Møller data.

The availability of two independent polarimeters was extremely useful. During the first run period, results from the Compton polarimeter first brought attention to potential issues with the Møller polarimeter, which later resulted in the discovery of the broken quadrupole. Cross checks of the two polarimeters were performed by making measurements at the same beam current (4.5 μA) – normally the Møller took data at $\approx$1 μA while the Compton operated at the nominal beam current of the experiment, 180 μA. An important by-product of this measurement was confirmation that the beam polarization measured at low beam currents is identical to that measured at high beam currents.

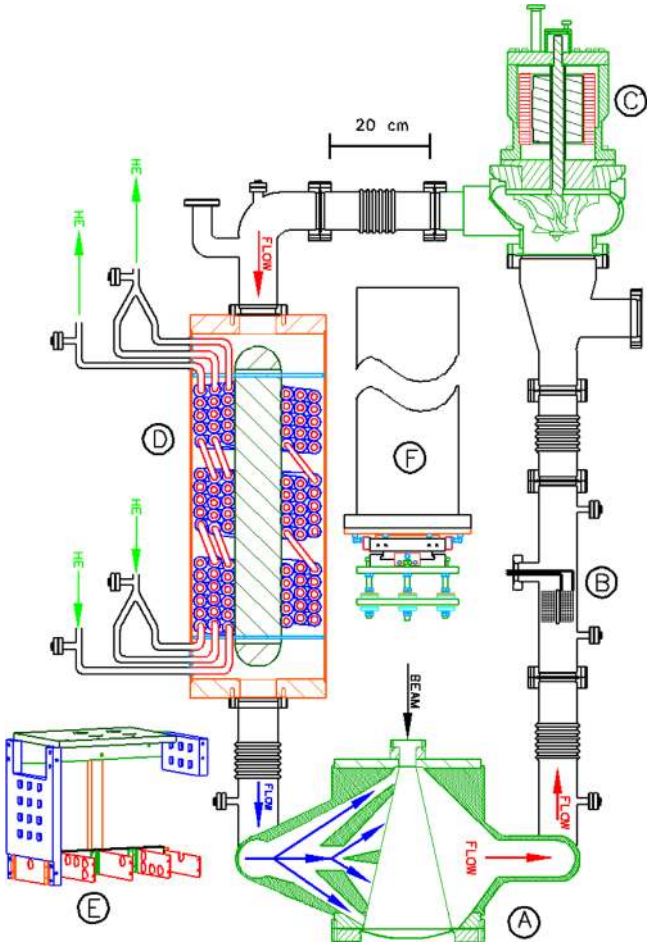

Fig. 16. A schematic showing the components of the Q_{weak} target. (A) The beam interaction cell (pitched 90° in this figure in order to illustrate the flow pattern), (B) the heater, (C) the centrifugal re-circulation pump, (D) the hybrid heat exchanger, (E) the solid target ladder, which was mounted directly below the cell, and (F) the long thin stainless steel pipe which mechanically supported the loop, as well as the manual cell adjustment mechanism at its lower end.

5. The liquid hydrogen target

The Q_{weak} liquid hydrogen (LH_2) target (see Fig. 16) consisted of a closed hydrogen loop whose main components were a pump to circulate the H_2, a HX[43] to liquify the H_2 and remove the heat deposited by the e^- beam, a cell with thin windows where the beam interacted with the H_2, and a heater to replace the beam power when the beam was off and to regulate the temperature of the H_2. The target was designed [59,60] to operate at 20 K and 207–228 kPa. It was connected at all times to storage/ballast tanks with a total volume of 23,000 STP[44] liters. The volume of LH_2 was $\sim$58 l.

The ionization energy loss of the 1.16 GeV electron beam traversing the 34.4 cm of LH_2 was 2.1 kW. A further 0.7 kW of cooling power was provided for viscous heating (180 W), pump heat (150 W), conductive and radiative heat load (150 W), as well as reserve power for the heater (250 W).

The target loop was affixed to a 1.6 m long stainless steel pipe (see Fig. 16 F) in an evacuated scattering chamber connected to the beam line. A small fast-acting gate valve isolated the chamber from the upstream beamline. The downstream end of the chamber was provided with a custom [61] 40.6 cm diameter, extended-stroke gate

[43] Heat eXchanger.
[44] Standard temperature and pressure.

valve which isolated the chamber from the downstream beamline as well as the thin downstream vacuum window on the chamber. The gate retracted into a lead box when the valve was open and the beam was on to protect the ethylene propylene diene monomer (M-class) rubber (EPDM) seals on the gate from radiation damage. A spoked aluminum 2024-T4 vacuum window with eight 0.89 mm thick windows was attached to the downstream flange of the gate valve. The scattered electrons passed through the open gate valve, through these windows, and into the collimation system on their way to the experiment's detectors.

5.1. Target components

The target cell's central LH_2 volume was a conical section oriented along the beam axis such that all electrons scattered less than 14° passed through the larger diameter exit window. This comfortably included scattered electrons in the experiment's $5.8^\circ < \theta < 11.6^\circ$ acceptance. The Al 2219 cell contained strategically segmented inlet and outlet manifolds (see Fig. 16A) which directed the flow of LH_2 transversely across the beam axis (at ~ 3 m/s) and toward the center of both windows (at ~ 7 m/s). The precise geometry of the cell and its manifolds was arrived at iteratively using CFD[45] simulations.

The 22.2 mm ϕ entrance window of the cell was 0.097 mm thick Al 7075-T6. The Al 7075-T6 exit window of the hydrogen cell was a 0.64 mm thick machined surface 305 mm in diameter with a 254 mm radius of curvature. The unscattered beam passed through a thin spot 15 mm in diameter and 0.125 mm thick at the center of the exit window. The LH_2 thickness seen by the beam between the entrance and exit windows was 343.6 mm (after correction for thermal contraction and pressure expansion), or 3.9% expressed in radiation lengths.

In order to provide the nearly 3 kW of cooling power required, a hybrid counterflow HX was built (see Fig. 16D) that made use of ~ 14 K helium coolant from the ESR[46] as well as ~ 5 K helium coolant from the CHL.[47] Typical target coolant mass flows were ~ 14 g/s (5 K source) and ~ 40 g/s (14 K source). The unusually high 14 K mass flow was achieved by recovering the unused enthalpy of the returning 5 K coolant to pre-cool the 14 K helium supply in the ESR.

The HX [62] was composed of 12.7 mm ϕ copper fin tube with 6.3 fins/cm. The fin tube was wound in three 15-turn layers contained in a 27.3 cm ϕ stainless steel shell 70.6 cm long. A 9.2 cm ϕ solid Al mandrel ran the length of the central axis of the cylindrical HX to divert the H_2 flow across the fin tubes.

The 3 kW capacity heater (see Fig. 16B) consisted of 1.83 mm ϕ nichrome wire wrapped in four 23-turn layers through perforated G10 boards. The total resistance (cold) was 1.3 Ω. A 60 V, 50 A Sorenson DC[48] power supply [63] was used to energize the heater. The power sent to the heater was determined by a PID feedback loop looking at the hydrogen temperature as well as the e^- beam current.

The LH_2 was circulated around the target loop with a home-made centrifugal pump rotating at typically 29.4 Hz (see Fig. 16C). The pump provided a differential pressure (head) of 7.6 kPa (11 m), and a LH_2 mass flow of 1.2 kg/s (17.4 ± 3.8 l/s) determined from measurement of the temperature [64] difference across the heater. The 220 kPa system pressure was well above the parahydrogen vapor pressure (94 kPa at 20 K) to mitigate cavitation.

The pump was made by adapting a commercial aluminum automotive turbocharger impeller and volute to an AC[49] induction motor [65]. Several turns of copper pipe carrying returning 20 K helium coolant were wrapped around a custom motor housing to help remove heat from the motor. Initially, bearings employing ceramic balls and race with a teflon retainer failed. They were replaced with bearings using ceramic balls, a stainless steel race, and graphite impregnated vespel retainers. The pump was further modified to promote a small flow of LH_2 across the bearings. One end of the motor shaft spun the 142 mm ϕ impeller, the other spun a small tachometer magnet.

5.2. Solid targets

A remotely controlled 2-axis motion system with 600 mm of vertical travel and 86 mm of horizontal travel was used to position the LH_2 target or any of 24 solid targets on the beam axis. The solid targets were distributed across three arrays in an aluminum target ladder assembly (see Fig. 16E) in good thermal contact with the bottom of the LH_2 target cell. Each target in the upper two arrays was 2.5 cm square. The lower array was composed of various combinations of foils in two rows and three columns at five (Z) positions along the beam axis between the upstream (entrance) and downstream (exit) LH_2 cell windows. The combinations of "optics targets" in this array were used to aid the development of vertex reconstruction algorithms at ~ 100 pA beam currents.

A second array of 12 targets arranged in four rows and three columns was situated at the same (Z) plane along the beam axis as the upstream window of the target cell. Likewise, a downstream array of six targets arranged in two rows and three columns was located at the Z of the exit window of the LH_2 cell. These two arrays were used for separate background subtraction of the upstream and downstream aluminum cell windows of the LH_2 target. Different thickness aluminum background targets were provided in both the upstream and downstream matrices to benchmark radiative corrections [66]. Targets of pure aluminum, thick and thin carbon targets, and beryllium were also provided. Other targets in these arrays were used to measure the relative location of the beam and the target system using a BeO viewer in conjunction with a TV camera looking at the targets, as well as thin aluminum targets with various size holes in their centers.

These latter hole targets were especially useful to position the target system with respect to the beam. One mm thick aluminum "hole targets" with two mm square holes punched out of their centers were moved into the beam. A 2-dimensional profile of the beam position at the target was generated using the dithering/raster magnets (described in Section 3.1). Only beam which missed the hole, and could thus scatter into the detectors generated a trigger (see Fig. 17). By measuring the hole profiles at both the upstream and downstream Z locations, the X, Y, pitch, roll, and yaw of the extended target could be accurately determined. Offsets in X and Y could be corrected in real time using the 2-axis motion system. Pitch, roll, and yaw offsets were corrected with a manual cell adjustment mechanism when the target was warm. The success of the target positioning achieved using the hole targets was confirmed after the experiment by inspection of spots left by the beam on the target cell windows as well as the solid targets. In all cases, the spots were well within 1 mm of the center of each target.

5.3. Target performance

Except for the early failure of the LH_2 pump bearings mentioned above, the target met expectations. About 8 h were required to condense the hydrogen in the target. Warming the target to room temperature (by stopping the coolant flow) took about 2 days.

The temperature PID feedback loop on the heater kept the target temperature at 20.00 ± 0.02 K while the beam was on. Damped oscillations of 100 mK were observed for 2–3 min when the 180 μA beam was interrupted. To improve temperature stability upon restoration of beam, the beam was ramped back to full current at the rate of 5 μA/s.

[45] Computational fluid dynamics.
[46] End station refrigerator.
[47] Central helium liquefier.
[48] Direct current.
[49] Alternating current.

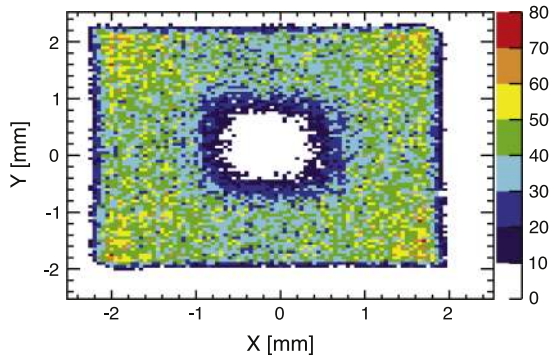

Fig. 17. Profile of the beam position on the hole target. The central area devoid of events represents the 2 mm × 2 mm hole in the target illuminated by a 4 mm × 4 mm dithered beam.

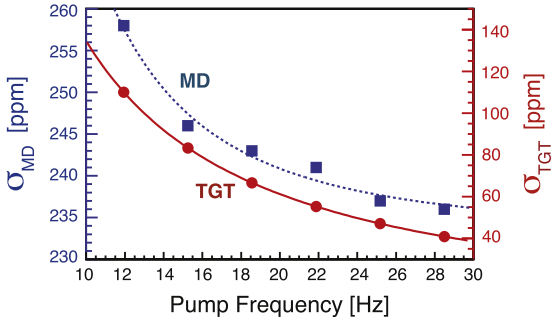

Fig. 18. The measured quartet-level main detector asymmetry width measured at varying rotational speeds of the LH_2 re-circulation pump (solid square points, dotted fit). The fit function is $\sigma_{MD}^2 = \sigma_A^2 = 233^2 + 1889^2/f^{2.288}$, where f is the pump frequency in Hz. Conditions were 169 μA with a 4×4 mm^2 raster. The solid circles and fit curve are the corresponding target noise results (right hand vertical scale) deduced assuming the variation in the main detector asymmetry width is due exclusively to varying target noise.

At high beam currents, the small bulk reduction of the nominal 71.3 kg/m^3 density of the LH_2 target was obscured by percent-scale nonlinearities in the main detector signal chain and the BCMs used to normalize the signals. A bulk LH_2 density reduction of 0.8% ± 0.8% at 180 μA was estimated by comparing changes in the detector yield as a function of beam current for the LH_2 and solid targets.

The target was also operated at a beam current of 2 μA with various pressures of cold H_2 gas, as well as with the target loop evacuated, in order to characterize the background from the cell windows.

The primary metric of target performance was its contribution to the main detector asymmetry width σ_A (measured over quartets), as discussed in Section 1.3. This contribution arises from target noise near the helicity reversal frequency and includes density fluctuations from all sources. Because of the high beam current employed in the experiment, fast helicity reversal was essential in reducing the ratio of target noise to counting statistics to a nearly negligible level.

The target noise was explicitly measured [67] using three independent techniques, by measurement of the asymmetry width in the main detectors as a function of either beam current, rastered beam spot size at the target, or the rotational frequency of the hydrogen re-circulation pump. The latter is the cleanest and surest method, however consistent results were obtained using all three methods. Results from one of the target noise studies are provided in Fig. 18. At the nominal conditions of the experiment (180 μA, 4×4 mm^2 raster, 28.5 Hz pump speed), the target noise was 53 ppm with an estimated 5 ppm uncertainty.

6. Collimation and shielding

The experiment was carefully designed to mitigate the extraordinarily high levels of radiation resulting from the use of a large beam current on a long target. Besides choosing radiation-hard materials (*e.g.*, Spectrosil 2000 synthetic quartz [68] for the detectors), and materials with relatively short half-lives when activated (*e.g.*, aluminum beamline components instead of stainless steel), two collimation systems and heavy use of shielding around the target area and the main detectors were employed. Portions of the collimator region shielding and the detector shielding hut are shown in Fig. 1.

6.1. Triple collimator

The main collimation system (see Fig. 1) consisted of a triplet of lead antimony (95.5% Pb, 4.5% Sb) collimators each with eight sculpted apertures that passed scattered electrons into each of the experiment's eight octants. The first was a cleanup collimator 15.2 cm thick centered just 74 cm downstream of the target center to provide initial cleanup. Its apertures were sculpted with 14 sides to allow electrons scattered from a hypothetical 9×9 mm^2 beam envelope anywhere along the target length to pass through the defining aperture of the second collimator. A pair of retractable 5 cm thick tungsten blocks could be positioned behind two opposing apertures of the first collimator to block scattered electrons for dedicated, intermittent background studies.

The downstream face of the second collimator defined the acceptance for scattered electrons. It was centered 2.72 m downstream of the target center, and was 15.0 cm thick. The electrons passed through eight six-sided openings, each approximately 400 cm^2 in area, defining an angular acceptance from the upstream end of the target of $\theta = 5.8 - 10.2^\circ$, and $\theta = 6.6 - 11.6^\circ$ from the downstream end of the target.

A third cleanup collimator 11.2 cm thick was located 3.82 m downstream of the target center, at the entrance to the magnet. It was sandwiched between aluminum plates for support. It provided several centimeters of clearance to the elastic electron profile.

6.2. Lintels

Lead lintels were installed between the coils of the magnet to shield the detectors from line-of-sight neutrals generated at the inner apertures of the defining collimator. The lintels were located 70 cm upstream of the magnet's center, with a size of 26.2 cm radially, 70 cm long between adjacent magnet coils, and 10 cm thick with a forward pitch of 20.85°. They provided 2 cm of clearance to the elastic electron envelope, and are discussed further in Section 11.2.

6.3. Beam collimator

The experiment was designed to minimize line-of-sight between the target and the aluminum beampipe in order to reduce backgrounds in the main detectors. Simulations showed that this could be almost completely achieved with a water-cooled tungsten–copper beam collimator 21 cm long fit snugly in the central aperture of the most upstream collimator. The upstream face of this 7.9 cm diameter beam collimator was attached to the central hub of the scattering chamber vacuum window only 47 cm downstream of the target cell's exit window. The beam passed through an evacuated tapered conical section machined out of the center of the collimator which was 14.91 mm in diameter at the upstream end and 21.5 mm in diameter at the downstream end. From there it was flanged to the downstream beamline. The power deposited on the beam collimator was ~1.6 kW, derived from the measured water flow and temperature difference across it.

The maximum angle $\theta_{max} = 0.88^\circ$ passed by the beam collimator corresponds to events scattered at the downstream face of the target

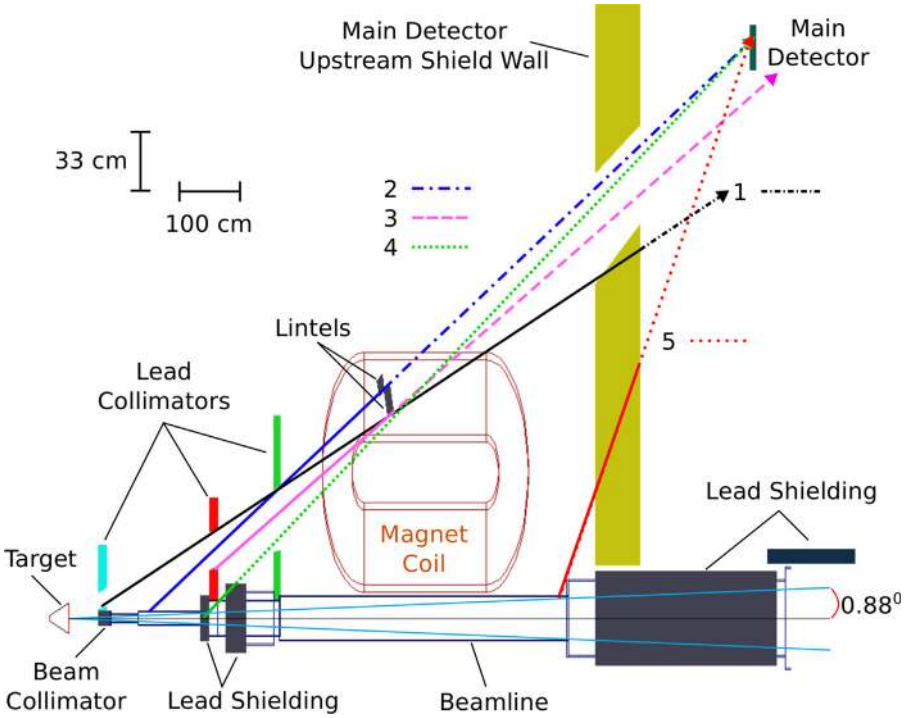

Fig. 19. A simplified cross-sectional elevation view through the beam axis illustrating the neutral background sources downstream of the target and how the main detectors were shielded from them. The vertical scale is amplified by a factor of three for clarity. The beam passes from left to right in this figure. Only the topmost main detector is shown, along with the corresponding neutral particle trajectories that were shielded as discussed in the text. The trajectories are represented as solid lines until encountering the shielding put in place to prevent them from reaching the main detectors, after which they are represented by different line types. The $\pm 0.88^{\circ}$ cone inside the beam pipe represents the maximum angle passed by the beam collimator for events generated on the downstream face of the target, as discussed in the text.

which intercepted the downstream aperture of the beam collimator. Including the corners of the 4×4 mm^2 square raster increases $\theta_{\max}$ to 1.11°. There were several regions along the downstream beamline which intruded on this cone, depicted in Fig. 19. Neutrals from the first region (ray 2 in Fig. 19) were mitigated by the lead lintels described in the previous Section 6.2. The lintels also blocked neutrals generated on the inner radius of the defining collimator apertures, represented by ray 3 in Fig. 19. The second region along the beamline (ray 4 in Fig. 19) was discovered during the setup period of the experiment, using dosimetry and trial shielding. It was at the upstream face of the defining collimator, aggravated by the presence of one of the two stainless steel bellows along the beamline downstream of the target. After the setup run, an additional 5.1 cm of lead shielding was clamped along 15 cm of the beampipe upstream of the defining collimator, and after Run 1 an additional 30.5 cm of lead was added along the beampipe downstream of the defining collimator. The third region was at the exit of the magnet (ray 5 in Fig. 19), just upstream of the detector hut shielding wall. This region was well shielded by the detector hut shielding wall, discussed next in Section 6.4, as well as by surrounding the entire length of beamline inside the detector shield hut with 5.1 cm of lead shielding. An additional (fourth) region along the beamline downstream of the main detectors was covered by the lead beamline shielding and did not contribute to the background. Finally, the main detectors were well shielded from neutral particles originating in the target by the triple-collimator system, as shown by ray 1 in Fig. 19.

6.4. Shielding

The region immediately downstream of the target scattering chamber between the first and second collimators was completely enclosed in concrete shielding 61 cm thick. Further downstream, the main detectors were enclosed in a separate shielding hut made of 122 cm thick concrete shielding with shielded entrances. The 80 cm thick upstream wall of this hut was formed from 10 tightly fitting interlocking sections. The sections consisted of high-density (2700 kg/m^3) barite loaded concrete (Ba_2SO_4). Stainless steel rebar (and stainless steel lifting fixtures) was used due to the proximity to the magnet. The apertures in this front wall provided several cm clearance for the elastic electron envelopes determined by the defining collimator, as shown in Fig. 20. The area around the beam-pipe penetration was filled with lead. The shielding hut downstream of the main detectors was made using 122 cm thick iron shielding blocks.

7. The spectrometer

The QTOR[50] magnetic spectrometer focused elastically scattered electrons within the acceptance profile defined by the triple collimator system onto eight rectangular fused silica detectors. Its design was loosely based on the BLAST[51] magnet [69], and provided a large acceptance for *ep* elastics and a high degree of azimuthal symmetry in an iron-free magnet to minimize parity-conserving A_{zz} backgrounds. The QTOR spectrometer spatially separated elastic and inelastic events at the focal plane. In conjunction with the triple collimator system, the spectrometer separated elastic events from line-of-sight trajectories (photons and neutrons) originating in the target. It also swept away low-energy electrons from the copious Møller interactions in the target.

The QTOR spectrometer consisted of eight identical resistive coils electrically connected in series and arrayed azimuthally around the beamline, centered 6.5 m downstream of the target. Each coil was composed [70] of a double pancake of 13 turns of copper conductor. Each racetrack-shaped pancake had straight sections 2.20 m long, and

[50] Q_{weak} toroid.
[51] MIT/Bates large acceptance spectrometer toroid.

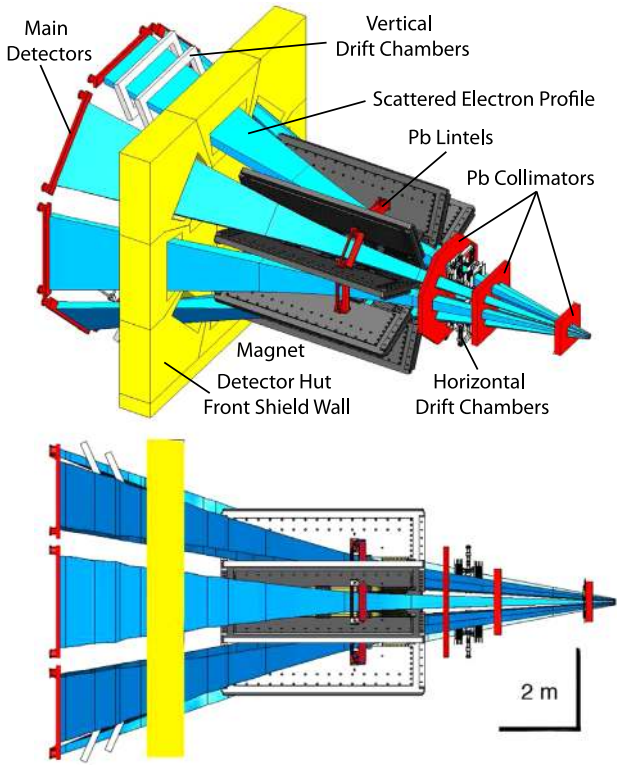

Fig. 20. CAD drawings showing the eight scattered electron profiles defined by the collimator triplet passing through the apertures in the detector hut upstream shielding wall. The upper figure is from a perspective similar to Fig. 1. The bottom figure is a cross-sectional view, with scales provided. In both figures the beam goes from right to left. The scattered electron profiles were obtained from Monte-Carlo simulations and then overlaid into the CAD model. They originate at the LH2 target and terminate on the eight synthetic quartz main detectors. The lintels between the magnet coils are also shown. The tracking chambers are depicted between the second and third collimators as well as downstream of the detector hut.

semi-circular curved sections of inner (outer) radius 0.235 m (0.75 m). The oxygen free, high-conductivity conductor was formed from long copper bars brazed together, of cross-section 5.84 cm $\times$ 3.81 cm with a central hole of diameter 2.03 cm for cooling water supplied at 13.3 l/s. The nominal resistance of each 3900 kg coil was 1.76 m Ω at 20 °C. The design current density was 500 A/cm^2. Each of the eight coils was mounted in an aluminum coil holder. The coil holders were in turn mounted in a large aluminum frame assembled with silicon–bronze fasteners to minimize magnetic material (see Fig. 2).

Due to the iron-free nature of the magnet, it did not have to be cycled through a hysteresis curve to obtain a reproducible field. The field was determined from a DCCT[52] at the output of a 2 MVA, $\pm$ 10 ppm current-regulating power supply [71]. A Hall probe was installed as a cross-check on the stability of the QTOR power supply current. This probe helped to identify intermittent periods when radiation damage affected the stability of the DCCT.

The shape of the magnetic field is depicted in Fig. 21. Electrons were deflected radially outwards by the magnet. At the mean scattered electron angle of 7.9°, the $\int B\,dl$ was about 0.9 T-m. The collimated elastic electrons in each octant were focused into an envelope which was roughly 10 cm tall in the dispersive direction, but almost 2 m wide in the non-dispersive direction at the position of the main detector array 5.78 m downstream of the magnet center. Due to ϕ-dependent aberrations, curvature of the elastic event envelope resulted in a mustache-shaped image on the focal plane, as discussed in Section 8.5.

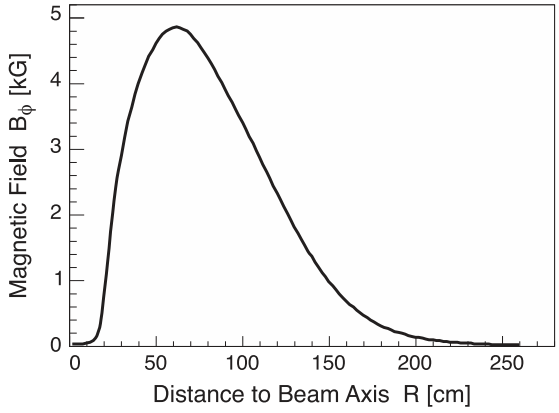

Fig. 21. Radial distribution of B_ϕ of the QTOR magnetic field magnitude at $z=0$ (the center of the magnet) and $\phi=0$ (halfway between the left two coils when looking downstream). The field is dominated by the azimuthal component B_ϕ. Its radial and axial components B_R and B_Z are small, however defocussing in the azimuthal direction was nevertheless large enough to double the required length of an individual detector.

The QTOR field was carefully simulated and techniques were developed to analyze the results of field mapping [70] carried out initially at MIT/BATES[53] using a 3-axis mapper. The mapper measured positions to $\pm$0.3 mm and magnetic fields to $\pm$0.2 G. It employed a 3-axis gantry that moved a probe over a 4 m $\times$ 4 m $\times$ 2 m range. The probe consisted of two high-precision 3-axis Hall effect transducers, temperature sensors, clinometers and photodiodes. Zero-crossing measurements of certain fringe field components as well as direct field measurements in the envelope of the scattered electron trajectories were performed. Simulations of the effects of coil misalignments (of ideal coils) indicated that they had to be positioned within $\leq$3 mm radially, and $\leq$0.1° azimuthally of their ideal positions. The QTOR magnet center had to be within $\leq$3 mm of the beam axis, and the eight field integrals along the electron trajectories had to be matched to within 0.4%.

The mapping indicated that the coil positions were well within the desired 3 mm of their ideal positions in X, Y, and Z of the magnet's local coordinate system, except for two coils that had $-$3.1 mm and 3.8 mm displacements in X, the radial outward direction. The measured coil average of the angular displacements in X, Y, and Z were 0.04°, 0.07°, and 0.14°, respectively. Z is along the axis of the spectrometer, and Y is perpendicular to the coil measured from its center. Measured coil-to-coil variations in $\int B\,dl$ were $\leq$0.3% except at the outermost radii of some of the coils, corresponding to the largest scattering angles and lowest scattered electron rates, where variations up to about 0.5% were found. Fig. 22 shows the difference between the average $\int B\,dl$ from all eight octants, and the calculated $\int B\,dl$ based on the actual coil positions determined from the zero-crossing measurements. This difference is plotted as a function of the azimuthal angle ϕ for several polar angles θ in each octant to illustrate the high degree of azimuthal symmetry achieved across the spectrometer. The QTOR magnet was fiducialized at MIT/BATES, transported to JLab and installed in experimental Hall C. After installation, the upstream half of the magnet was remapped and calibrated to verify the alignment and magnet performance.

7.1. Spectrometer performance

During the Q_{weak} experiment, QTOR was operated routinely at a current of 8900 A DC (123 V). The cooling water temperature rose $\sim$20 °C across the magnet. Some problems were experienced early in the experiment due to cooling water restrictions, which

[52] DC current transformer.

[53] Bates linear accelerator center.

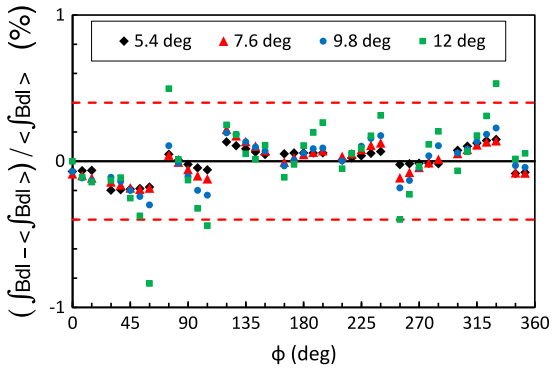

Fig. 22. Relative difference $(\int B\,dl - \langle \int B\,dl \rangle)/\langle \int B\,dl \rangle$ between the eight-octant average $\langle \int B\,dl \rangle$ and the calculated $\int B\,dl$ for each octant based on the actual coil positions as determined from the zero-crossing field mapping measurements. The results for each octant are plotted as a function of the azimuthal angle ϕ for the four different polar angles θ indicated in the legend. $\phi=0$ corresponds to the center of the top octant, and increases going clockwise around the beam axis. The dashed lines indicate the specification on this parameter. Note that the smallest and largest polar angles plotted are just outside the scattered electron acceptance defined by the collimation system. The same is true for the azimuthal range.

led to burst cooling hoses and even a burst water cooled lead which damaged the load sensing resistors in the power supply. A phase failure in the power grid damaged the DCCT, which was repaired, recalibrated, and checked using the Hall probe. A blown silicon-controlled rectifier in the power supply and a bad breaker in the 2 MVA service feed also caused significant down time. Radiation damage to the power supply was mitigated with the addition of steel shielding. The intense flux of low-energy electrons from Møller scattering was deflected radially outward and away from the magnet by the magnetic field. Furthermore, the magnet coils themselves were in the shadow of the collimation system, and thus received a radiation dose far smaller than the 1 Mrad seen by the main quartz detectors.

A combination of glass witness plates (which recorded the location of the beam envelope through radiation damage induced darkening) and the tracking chambers verified that the eight beam envelopes were radially symmetric within ± 0.5 cm. However, the nominally field-free region along the central symmetry axis (see Fig. 21) contained small contributions amounting to ~ 5 kG cm, which arose from minor misalignments of the magnet coils. Although this had no effect on the scattered electrons of interest in the experiment, it did steer low-energy electrons in the beam pipe towards the 2 o'clock position looking downstream, breaking the azimuthal symmetry in the downstream luminosity monitors described in Section 8.4.2. A more serious consequence was the resulting ~ 1 kW beam power deposited on a flange near the end of the beamline (~ 14 m downstream of the magnet center) which led to vacuum leaks, and impacted the experiment's efficiency in Run 1. This section of downstream beamline was redesigned for Run 2, cooling was added, and the vacuum problems were eliminated.

8. Integrating mode electron detectors

In addition to the eight main detectors which were used to measure the experiment's main quantity of interest, the elastic asymmetry defined in Eq. (2), several ancillary detection systems were also employed. Dedicated background detectors helped monitor and quantify backgrounds and their asymmetries. A focal plane scanner was used to map out the profile of events in 1 cm^2 pixels over the face of one of the main detectors at the full current used in the experiment. Upstream and downstream arrays of luminosity monitors were also used.

8.1. The main Cherenkov detectors

The challenges associated with the main detector were to detect elastically scattered electrons in integrating mode with low noise, low background, high linearity, and excellent azimuthal symmetry and radiation-hardness over a focal plane area totaling several square meters. The main detector system [72] employed a set of eight Cherenkov detectors made of non-scintillating, low-luminescent synthetic quartz bars (Spectrosil 2000 fused silica [68]) which were extremely radiation-hard and insensitive to neutral backgrounds. Each detector consisted of two 100 cm $\times$ 18 cm $\times$ 1.25 cm radiators (made by Saint-Gobain Quartz [73]) and two 18 cm $\times$ 18 cm $\times$ 1.25 cm long light guides (made by Scionix [74]). All surfaces were finished with 25 Å (RMS) surface polishing. The systematic point-to-point variations in thickness were ± 250 μm. All edges were beveled to a width of 0.5 mm to reduce chipping. Pairs of bars and lightguides were glued together end-to-end, forming 240 cm long bars with three main glue joints: light guide-to-radiator, radiator-to-radiator, and radiator-to-light guide (see Fig. 23). The index of refraction of the quartz was $n=1.482$ at a wavelength of 280 nm, corresponding to a threshold $\beta=0.67$ and a Cherenkov cone angle of 47.6°.

The detectors were instrumented with 130 mm diameter PMTs on each end of each detector bar. Each PMT (Electron Tubes 9312WKB [75]) had a multi-alkali S20 (Na_2KSb:Cs) photocathode, UV transmitting glass window and DC coupling with an electrostatic shield at cathode potential. The PMTs had 10 stages of high-gain, high-stability SbCs dynodes with a linear focus design for good linearity and timing. They were sensitive in the wavelength range from 200 to 900 nm, with a peak quantum efficiency of about 23% at 260 nm, well matched to the Cherenkov light wavelengths in quartz. Each PMT was magnetically shielded using a double-layer mu-metal case.

The PMTs were glued onto the downstream faces of the light guides. The optical glue used to attach the quartz pieces and the PMTs was SES406 by Shin-Etsu [76]. This glue was chosen for its mechanical strength and stable light transmission under high radiation doses. Both the quartz and the glue were tested for radiation damage at doses up to 1 Mrad at a ^{60}Co facility [77], approximately the dose they were expected to receive over the course of the experiment.

To suppress soft neutral backgrounds, a 2 cm thick lead preradiator was installed in front of each quartz bar. This increased the light yield by a factor of seven and improved the signal-to-background ratio by ~ 20, although shower fluctuations in the pre-radiator also introduced an additional excess noise ($\sim 10\%$) to the total asymmetry width.

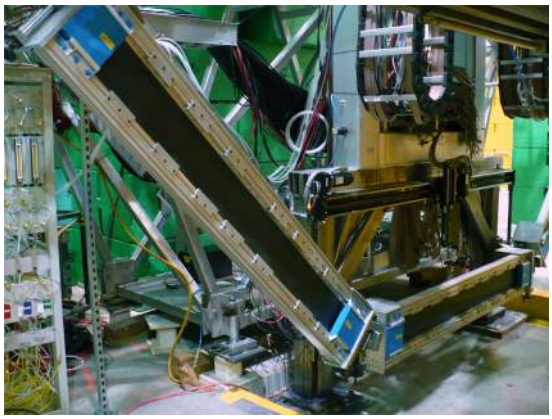

Fig. 23. Two of the eight main detectors, before installation of the lead preradiators. The squares standing out on each end of the detectors are lead shielding covering the light guides and PMTs. The quartz sampling scanner is also shown above the lower detector in the figure.

The eight quartz Cherenkov detectors were arranged symmetrically about the beam axis (3.44 m from the beam axis to the outer edge of each bar) at the focal plane of the spectrometer (5.78 m downstream of the center of the QTOR magnet). The mounting and support structure consisted of a housing for each quartz and PMT assembly, an exoskeleton around each housing, and a general support structure for all eight detectors, referred to as the Ferris wheel. Each light-tight housing consisted of an aluminum frame which supported the quartz bars and the PMTs, and thin PORON® covers [78]. The housing was mounted inside the exoskeletons, which reinforced the mechanical strength of the main detector housings and provided mounting structures for the pre-radiators and PMT shielding. Lead plates 5 cm thick were mounted on the exoskeleton just in front of the PMTs and at their inner radius side. This provided 10 radiation lengths attenuation for $\mathcal{O}(1)$ GeV particles (electrons) coming from the upstream direction and from the beamline. The exoskeletons also provided the mounting interface to the overall support structure (the Ferris wheel). The Ferris wheel located the main detectors at the desired radius in the focal plane. The attachment of the exoskeletons to the Ferris wheel incorporated manual radial motion capabilities with a range of about 15 cm.

The Ferris wheel also supported cable trays and access platforms with ladders. All the mechanical structures were built with aluminum in order to provide a "low-Z" and iron-free environment around the detectors. The entire detector system was placed in a shielded hut (see Section 6) to reduce the background.

Cherenkov light generated by scattered electrons traveled along the quartz bar via total internal reflection and was collected at each end by the PMTs. An average of 98 p.e.[54] s were generated for each incident electron. The Cherenkov signals were read out with two types of custom made PMT bases: one for high-gain (2×10^6) event-mode calibration running at nA level beam currents and one for low-gain (~ 440) integrating-mode production running for asymmetry measurements at beam currents up to 180 μA. The low-gain operation in integrating mode reduced non-linearity effects from the PMT. This was achieved by using only the first seven dynode stages and keeping the remaining stages and anode at the same bias voltage as dynode 7, as well as operating the PMT at a relatively low bias of around -1 kV.

8.2. Integrating mode detector performance

The rate of scattered electrons incident on each of the eight main detectors was over 850 MHz, precluding the counting of individual events. Instead, the raw current of each of the 16 PMTs was read out using the electronics described in Sections 10.1 and 10.2 and saved for later analysis, which included pedestal subtraction and beam charge normalization (see Fig. 24). Pedestal data were acquired every 8 h by taking 1–5 min of data with no beam in the experimental hall. The RMS width of each tube's raw pedestal distribution over a typical 5 min period varied between 0.20 and 0.25 mV. More interesting was the width of the HC pedestal differences measured over helicity quartets, which was only 30 μV. That may be used to estimate the electronic noise contribution to the main detector asymmetry width as 5 ppm (relative to the nominal 6 V signal magnitude). This is negligible compared to the overall main detector asymmetry width of 230 ppm, which was dominated by the statistical width as described in Section 1.4. Similar results were obtained by replacing the detector inputs to the ADCs with a 9 V battery.

These pedestal data also provided an opportunity to search for a false asymmetry in the main detector signal chain due to electronic pickup. Helicity-dependent changes in the mean value of the pedestals were searched for and excluded with a typical sensitivity of ± 10 nV per monthly Wien setting. Given the signal magnitude of ~ 6 V, this meant that any false asymmetry from HC pedestals was <2 ppb per Wien setting. Because this method regularly tested the actual detectors, electronics, and current monitors (albeit necessarily at low duty factor), it was complementary to measurements by the continuously monitored battery signals which provided a 1 ppb limit on electronic pickup in the PMTs or PMT gating every 8 h.

The health of the 16 individual PMTs was tracked continuously so that damaged hardware could be identified and replaced. Fig. 25 displays how a typical PMT yield changed over the course of the entire Q_{weak} running period. Drifts in the detector yield over time scales of hours were typically 1% due to PMT gain drifts arising from

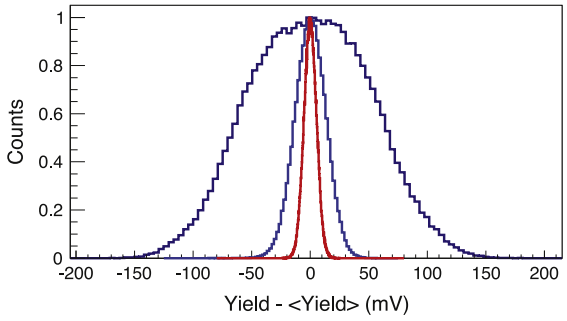

Fig. 24. A typical 6 min main detector PMT yield distribution after subtraction of the mean value of the yield. The outer ($\sigma=50.3$ mV) distribution corresponds to the raw signal and the middle ($\sigma=13.4$ mV) peak are the same data after normalization to the beam current. The innermost peak is a Gaussian distribution with a width corresponding to a calculated estimate of the shot (statistical) noise, which experiences no gain drifts due to factors such as temperature changes like the former two yield curves do.

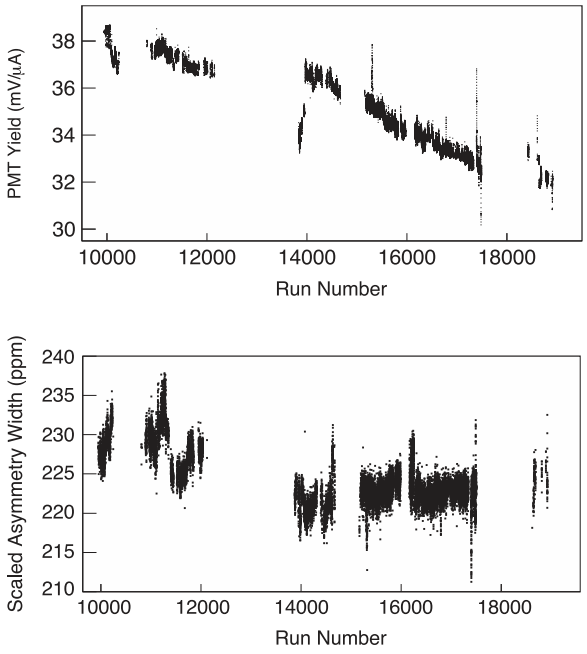

Fig. 25. *Top*: typical charge normalized main detector phototube yields over the course of the experiment. Run 2 started around run 14,000. The $\sim 10\%$ decrease in yield over time is attributed to gain degradation. The change at run 14,000 corresponds to a period when the beam current was raised as Run 2 got underway. Spikes near runs 15,500 and 17,500 are the results of temporary issues with heat dissipation in the BCM and DAQ electronics, respectively. *Bottom*: The main detectors' asymmetry width over the whole experiment, scaled by $\sqrt{(I/180)}$, where I is the beam current in μA. As described in the text, this metric combines detector, target, and BCM performance as well as regression to correct for HCBA.

[54] Photo-electron.

temperature variations in the hall, while a 10% gain degradation was observed over the course of all of Run 2.

The primary metric used to assess detector performance was the width of the asymmetry distribution (see Section 1.3). The general health of the experiment as a whole could be monitored by ensuring that widths in excess of counting statistics could be attributed to known sources such as the BCM resolution and target density fluctuations. For a 175 μA run, the average single-PMT asymmetry width (averaged over helicity quartets) was ~ 680 ppm. The full 16-tube (8 radiator) combination width was ~ 230 ppm. Fig. 25 (bottom) shows how the asymmetry width of the average of all 16 PMTs varied over the whole experiment.

Potential additional sources for increased asymmetry widths are non-linearities either in the detectors (hardware and electronics) or the BCMs. The inherent non-linearity of the main detector PMTs and associated electronics was studied in detail prior to the experiment with LEDs, with a non-linearity of $\sim 0.8\%$ at the signal levels corresponding to those experienced during the experiment.

8.3. Event mode electron detectors

The low-gain bases of the main detectors were swapped out with high-gain bases in order to use them at low beam currents (50 pA–200 nA) in an event-by-event counting mode. Further amplification ($\times 20$) was provided locally before each signal was sent to the counting room electronics outside the experimental hall. This configuration provided pulse height, timing, and coincidence information to be used in conjunction with drift chamber information to reconstruct kinematic quantities such as Q^2 and scattering angle. Data taken in this configuration also proved useful in calibrating the performance of individual phototubes. Comparisons of data acquired using LEDs with data obtained from scattered electrons in event mode were used to determine the number of photoelectrons generated per event. These numbers varied by 8–18 p.e./PMT from the average value of 98 p.e.s per event. The light collected from an event near the middle of the bar was about 2/3 of the light collected from an event near the end of the bar.

Timing information from the main detectors was also used both in track reconstruction as well as for systematic measurements of dilution factors for various background processes. By requiring a coincidence for events recorded by tubes on opposite ends of a single quartz bar, accidental events could be suppressed.

8.4. Luminosity monitors

The luminosity monitors (lumis[55]) were auxiliary detectors located where the scattered flux was much higher than at the main detectors, while the expected physics asymmetry of the contributing processes was much smaller than at the main detectors. Two sets of detectors – the upstream and downstream luminosity monitor arrays – were used during the experiment. The desire for a high scattered flux required the detectors to be in areas where they received a large radiation dose. The extra efforts to make these detectors radiation-hard worked very well. Both the upstream and downstream luminosity monitors made use of rad-hard Spectrosil 2000 quartz (fused silica) radiators [68]. Special signal connectors (Kings teflon [79]) on the PMTs were used to avoid the especially radiation sensitive insulators on standard BNC connectors. Long light guides helped distance the PMTs from the radiation field. The light guides were formed from single sheets of highly reflective aluminum (Alanod Miro-Silver 27 [80]) and continuously flushed with N_2 gas to eliminate the corrosive effects

[55] Luminosity monitors.

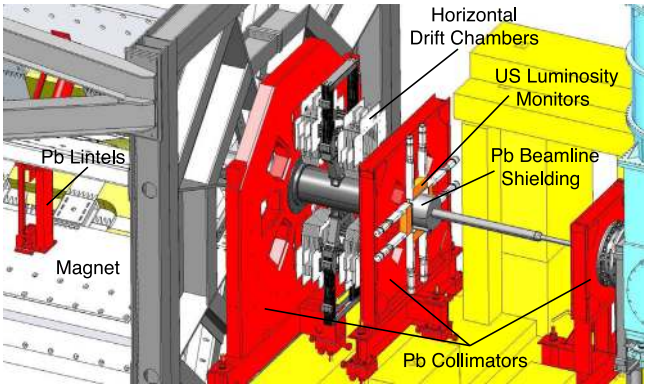

Fig. 26. A CAD drawing of the triple collimation region. The target is in the scattering chamber on the right side of the drawing; the beam direction is to the left. The lead collimators and the lead lintels between the magnet coils are shown in this view. The horizontal drift chambers are shown just upstream of the third collimator. The four upstream luminosity monitors are shown mounted to the upstream face of the middle collimator, each with two light guides and PMTs. The active elements span the light guide pairs in the horizontal and vertical octants.

of moist air and to reduce backgrounds. Pre-amplifiers located close to the detectors were heavily shielded with lead. Careful alignment was performed early in the experiment before activation made personnel access problematic.

8.4.1. Upstream luminosity monitors

The upstream lumis (see Fig. 26) were intended to provide a way to measure target noise if other methods failed to do so. As it turned out, the target noise was small and well measured by three other techniques (see Section 5.3). However, the upstream lumis were a crucial tool to link together beamline background asymmetries observed with differing configurations of other background detectors in the main detector shielding hut (described in Section 8.6).

The four upstream lumis [81] were Spectrosil 2000 quartz radiators [68] measuring 7 cm $\times$ 27 cm $\times$ 2 cm. They were situated 2.67 m downstream of the target on the upstream face of the defining collimator at a scattering angle of about 5° where they were expected to be primarily sensitive to Møller electrons. The detectors each saw a rate of about 115 GHz (scaled from event mode to a beam current of 180 μA), about half of which came from sources other than the target. They were read out with 5.1 cm diameter Hamamatsu R375 quartz window phototubes [82] operated in vacuum photodiode mode (unity gain voltage divider) at each end. The light from the detectors was transmitted to the PMTs through 35 cm long N_2 filled light guides. The remainder of the integrating-mode electronics chain is described in Section 10.2. The unity-gain bases were swapped with modest-gain ($\sim 10^6$) bases so that they could be used as relative beam current monitors in event (pulse counting) mode during the low beam current running.

8.4.2. Downstream luminosity monitors

The downstream luminosity monitors were situated 17 m downstream of the target at an angle of 0.5°, sensitive to similar rates of scattered electrons from Møller ($e-e$) and Mott ($e-p$) interactions in the target. Based on pure counting statistics considerations, these detectors were anticipated to have a smaller asymmetry width than the main detectors. In practice, their asymmetry width was only slightly smaller (~ 200 ppm typically) than the main detectors. Target (53 ppm) and BCM (60 ppm) noise contributed in quadrature to the anticipated statistical width (14 ppm). Excess noise from a variety of sources, including the beamline and beam monitor resolution, also contributed to the observed 200 ppm asymmetry width. However, they provided sensitivity to false asymmetries at this level,

because the expected asymmetry from the contributing physics processes was much smaller than that of the main detector. The relation of false asymmetries measured in these detectors to any potential false asymmetries in the main detectors is being studied. They also proved useful as beam current and relative position monitors during the extremely low current running used for the event mode of the experiment.

Each of the eight downstream lumis [81] consisted of a piece of Spectrosil 2000 quartz [68] measuring 4 cm $\times$ 3 cm $\times$ 1.3 cm with a 45° taper at one edge. Each of the quartz radiators had a 2 cm thick lead pre-radiator in front of it to suppress low energy backgrounds. They were inserted into flanged cups which penetrated the 61 cm diameter beampipe to within 13 cm of the nominal beam axis. Each quartz piece was read out with the same type of phototube and light guide described in Section 8.4 for the upstream lumis, using the integrating mode electronics described in Section 10. Fig. 27 displays how a typical downstream luminosity monitor phototube yield behaved over the course of the Run 2 period. As with the upstream lumis, the unity gain bases were swapped with modest gain ($\sim 10^6$) bases during the low beam currents used in the event mode of the experiment. The downstream lumis each saw about 150 GHz of scattered electrons (scaled up from event mode measurements) and withstood a dose of about 2 Grad over the life of the experiment.

8.5. The focal plane scanner

In order to measure the profile of events reaching the main detectors over the whole 4–6 orders of magnitude of beam current used in the experiment, a small scanning Cherenkov detector was built [83]. It provided confirmation early in the experiment that the scattered electron envelope on the main detectors agreed with simulations. It consisted of two overlapping 1 cm^3 cubes of synthetic quartz (Spectrosil 2000) fused silica Cherenkov radiators [68]. The geometrical overlap of the two sensitive elements formed a small fiducial area of 1×1 cm^2 to cope with the maximum electron flux of about 1 MHz/cm^2, allowing operation in event mode at most beam currents. Each quartz radiator was optically coupled via a 50 cm long air-core light guide to a Photonis XP2268 5 cm PMT. The light pipes were lined with highly specular Alanod Miro4 reflector [84], providing a light transport efficiency better than 93%. The two PMTs were read out in coincidence. Accidental coincidences were reduced by configuring the light guides in a non-overlapping V-shape. Despite configuring the air light guides in the super-elastic region, they were exposed to a large photon flux from the upstream beamline which contributed to a larger than expected accidental rate.

A 2D linear motion system [85] was employed to move the scanner detector along a predefined path while measuring position-dependent

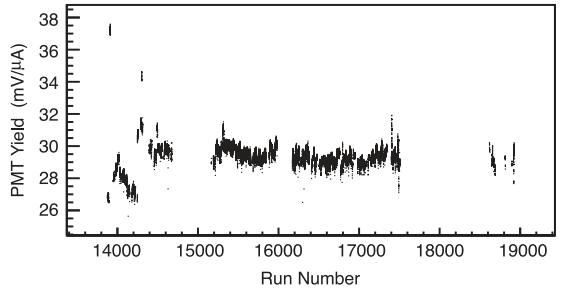

Fig. 27. Typical charge normalized downstream luminosity monitor yields over the course of Run 2 of the experiment. The behavior was typically very stable with no long-term gain degradation observed. Discrete jumps near the beginning of the running period were the result of deliberate beam position changes of ~ 0.5 mm during studies to determine the experiment's neutral axis. The relatively large size of the jumps reflects the expected large beam position/angle sensitivity of these very forward angle monitors.

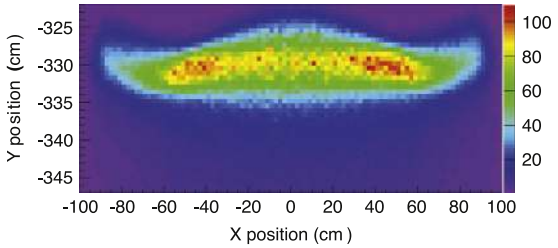

Fig. 28. Scattered electron flux distribution in the bottom octant obtained by the scanner. The *x*-axis is in horizontal direction, the *y*-axis is in vertical direction. The scale indicates the relative electron flux.

rates. The 2D linear motion system consisted of two stainless steel ball-screw driven tables with a range of 200 cm $\times$ 26 cm and a position resolution of 100 μm. The moving tables were driven by servo-motors controlled by a custom-built control box housing two Danaher S300 servo-amplifiers [86] and a Galil DMC-4020 motion controller [87]. Two linear displacement draw wire potentiometer position sensors [88] measured instantaneous detector positions. The ~ 500 mR/h radiation field inside the shielded main detector hut required the controller to be shielded with lead. A full scan (see Fig. 28) could be completed in half an hour when the detector was moved ~ 6 cm/s.

8.6. Background detectors

To continuously monitor the asymmetry of the diffuse background and search for potential leakage of the helicity reversal signal, a set of background detectors were constructed and placed at specific locations in the detector hut. The background detectors included one complete main detector assembly (identical to the other eight main detectors) placed in the super-elastic region, just downstream of the nominal focal plane as a beamline background monitor, and three smaller dark boxes numbered from 1 to 3.

Background detectors 1 and 2 consisted of a dark box containing a bare PMT of the same type as the main detector PMTs, shielded with double layers of mu-metal, an integrating-mode PMT base and an LED light source. Background detector 1 was placed in a well-shielded fixed location. Its LED light, PMT, and low-gain base delired a low-noise signal (~ 10 ppb over 8 h) to provide a noise floor reference for the main detector electronics chain. It was used to search for leakage of the helicity reversal signal, and thus needed to have similar cabling to the main detectors while being well-shielded from beam induced backgrounds.

Background detector 2 was moved in the super-elastic region next to different main detector PMTs to characterize the "PMT background" at each PMT. Background detector 3 was identical to 1 and 2, but had a piece of fused quartz (identical to the light guide extension used on the main detectors) glued to it in the same configuration as the PMTs were glued to the light guides in the main detectors. Background detector 3 was also moved in the super-elastic region next to the PMT of any of the main detectors to serve as a "PMT+lightguide background" detector. The LEDs in background detectors 2 and 3 were used only for checkout. Background detectors 2 and 3 both measured the asymmetry of the diffuse background, and needed to be close to a main detector radiator to measure the relevant background, ideally while minimizing cross-talk due to showering.

9. Event mode detectors

The tracking system was used for calibration measurements performed with low beam currents (50 pA–200 nA) to extract the acceptance-weighted average of Q^2 ($\langle Q^2 \rangle$) of the asymmetry measurement. $\langle Q^2 \rangle$ was formed from the measured scattering angle and

scattered momentum distributions, the analog response of the main Cherenkov detectors, the known incident beam energy, and a detailed GEANT 4 [89,90] simulation including all radiative effects. The tracking system was also used to characterize various backgrounds and monitor the performance of the main Cherenkov detectors.

To accomplish this, horizontal drift chambers (HDCs[56]) were used on the upstream side of the QTOR magnet, and vertical drift chambers (VDCs[57]) on the downstream side. HDC and VDC designs are distinguished by the dominant drift direction relative to the wire planes. In an HDC the ionization electrons drift parallel to the wire plane, and in a VDC they dominantly drift perpendicular to the wire plane. Scintillation counters were placed between the VDCs and the main detectors. During integrating mode, all the tracking detectors were retracted from the experiment's acceptance. During event-mode running, two octants at a time (180° apart) were instrumented with tracking detectors. Separate rotation systems were employed for the HDCs and the VDCs to rotate the chamber systems around the beam axis to cover each of the four octant pairs. One octant pair could be covered with either of the two sets of chambers for redundancy. The tracking system consisted of eight chambers and two scintillators: two VDC chambers, two HDC chambers, and one scintillator in each of the two octants.

During the tracking measurements, the HDCs were used in conjunction with the VDCs at beam currents of 50 pA on the 35 cm LH_2 target. The $\sim$100 kHz rate observed in the HDCs was dominated by $\sim$50 MeV Møller electrons which were swept away by QTOR before they reached the VDCs or the main detectors. The elastically scattered electrons of interest typically had a rate of $\sim$200 Hz under these conditions. Data were also obtained with various thin solid targets under similar conditions to study backgrounds and to tune the track reconstruction algorithms.

9.1. The horizontal drift chambers

For elastic scattering, ignoring radiation and energy losses, the four-momentum transfer squared Q^2 is given by

$$Q^2 = 2E^2\frac{(1-\cos\theta)}{1+\frac{E}{M}(1-\cos\theta)} \tag{9}$$

where M is the proton mass, E is the known incident beam energy, and θ is the lab scattering angle. The (HDCs) established the scattered electron trajectory before the magnet in the event mode of the experiment. They tracked back to the target to establish the interaction vertex and scattering angle θ required for determining the Q^2 distribution.

A total of five HDCs were constructed, with the fifth one serving as a spare. Each chamber consisted of six wire planes with 32 sense wires (20 μm diameter gold-plated tungsten wires strung at a nominal tension of 20 g) and 33 field wires (75 μm gold-plated beyllium-copper wires strung at a nominal tension of 30 g) per plane. The wire pitch was 5.84 mm, and the spacing between wire planes was 19.0 mm. The frame material was Ertalyte [91]. The six wire planes were in a $XUVX'U'V'$ configuration, with the U,V wires at angles of $\pm$53.1° relative to the X wires. In the installed orientation, the typical electron track made an angle of $\sim$7° relative to the normal of the wire planes, so there was no need to offset identically strung planes by a half drift cell to resolve the left-right ambiguity. An automated scanning system with a digital camera and the standard vibrating wire technique [92] was used during chamber construction to measure wire positions and tension, with typical standard deviations of $\sim$50 μm for deviations of wire positions from expected and $\sim$3 g for wire tension about nominal. The wire planes were separated by cathode planes made of double-sided aluminized mylar foil. The active area of each chamber was 28 cm $\times$ 38 cm. The operating gas mix was 65% argon–35% ethane. The cathode planes and field wires were held at a potential of $-$2150 V, while the sense wires were held at ground. Each completed chamber was tested with cosmic rays, with measured position resolutions of 150–200 μm, and single plane efficiencies of $>$99%. The single-wire position resolution was determined from the difference of a given wire's drift distance to the distance expected from a straight-line fit to $\sim$12 wires in a typical two-chamber HDC track. A typical residual obtained during running under nominal conditions ($\sim$50 pA beam current on the LH_2 target with $\sim$100 kHz chamber rate) is shown in Fig. 29.

9.1.1. HDC positioning system

The HDCs were situated between the defining (second) and third lead collimators just upstream of the QTOR magnet. Each of two octants was covered by a pair of chambers which constituted an arm. The two chambers which formed an arm for a given octant were separated by 42 cm; the upstream (downstream) chamber center was 3.15 m (3.57 m) from the center of the target.

Each arm could be positioned radially inward to cover a given octant during tracking measurements, or outward to clear the scattered electron acceptance during production running. Furthermore, the arms were attached to a central hub which rotated about the beam pipe. The two arms were fixed 180° apart. Each arm could cover one of the five different octants, which means that together both arms covered all eight octants, and that two octants could be covered by both arms (at different times). The HDCs were positioned radially and rotated about the beam axis manually.

9.1.2. HDC electronics

On-board Nanometric N-277 preamplifier/discriminator cards [93] sent the signals from each sense wire $\sim$27 m over twisted pair ribbon cable to TDCs[58] located in a hermetically shielded electronics hut in the experimental hall. The TDCs used were the JLab F1TDCs [94], which are high-resolution multi-hit TDCs in 64-channel VME modules.

9.2. The vertical drift chambers

The VDCs were used in conjunction with the tracks from the HDCs and the known magnetic field of QTOR to determine the scattered momentum and thereby identify elastically scattered electrons.

A total of five VDCs were constructed, with the fifth serving as a spare [95]. The chambers were patterned on an earlier design used in JLab's Hall A for many years [96], but with an increase in overall size as well as modifications to some materials and other details which made them more cost effective and gas tight.

Each chamber consisted of two anode wire planes held at ground potential. Each plane included 279 sense wires. The sense wires were 25 μm diameter gold-plated tungsten wires strung at a nominal tension of 60 g. The wire pitch was 4.97 mm. The two wire planes per chamber were strung in a UV configuration, with the U and V wires oriented at angles of $\pm$26.56° from the long axis of the chambers.

High voltage (HV[59]) cathode planes operated at $-$3800 V were situated 12.7 mm above and below each wire plane. The outer HV planes were 12.7 μm thick Mylar foils, aluminized on one side. The HV plane located between the two wire planes was the same material but was aluminized on both sides.

The frame material, used for both the wire planes and the HV planes, was 1.27 cm thick G10-FR4 [97], a mesh of compressed glass

[56] Horizontal drift chambers.
[57] Vertical drift chambers.
[58] Time to digital converters.
[59] High voltage.

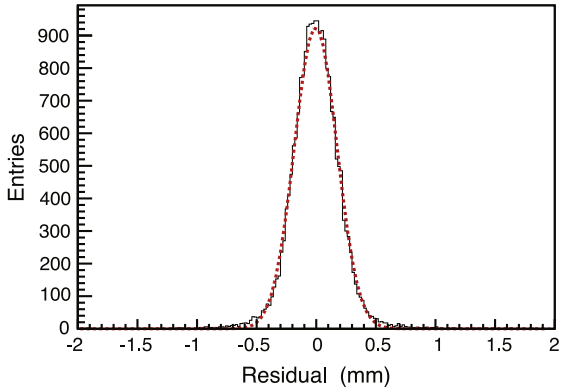

Fig. 29. HDC track fit residuals under nominal running conditions (see text). Displayed are the track fit residuals for a single plane of a 12-plane track fit through two HDCs. The dashed line is a Gaussian with RMS = 178 μm, which is a measure of the characteristic chamber resolution.

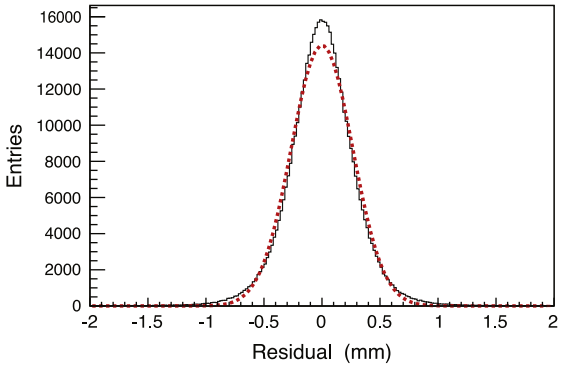

Fig. 30. *Solid curve*: A typical single-wire position residual formed from ~24-hit tracks in the VDC (typically six wires firing in each of two planes in each of two chambers). *Dashed curve*: A Gaussian fit to the data, with standard deviation of 264 μm. The RMS width of the data is 295 μm.

fibers and epoxy/resin. The frame pieces were sand-blasted to create a smooth, uniform surface to ensure uniform spacing between the cathode planes and the sense wires. Each rectangular frame (235 cm × 84 cm) was made of four separate pieces doweled together and bonded with Araldite epoxy (AY 103 resin and HY 199 hardener). The active area for each chamber was 204.5 cm × 53.3 cm. The entire 10.2 cm thick stack of frames was held together by two 1.9 cm thick aluminum tooling plate frames with central cut-outs. About 12.7 μm thick aluminized Mylar foils were stretched across the aluminum frames to contain the 50% argon and 50% ethane gas mixture.

An automated scanning system with a CCD[60] camera attached to a stepper motor and linear encoder, and the usual vibrating wire technique [92] were used during chamber fabrication to measure wire positions and tensions. With respect to the nominal values (4.97 mm pitch, 60 g tension), typical standard deviations were 78 μm and 5.6 g, respectively.

Each completed chamber was tested with sources and cosmic rays. The dark current (current from cosmic ray flux alone) was ~100 pA. The gas gain was determined to be $\sim 2 \times 10^5$ at the operating voltage (−3800 V). The single-wire efficiency was >98.8%. At the ~50 pA beam current used for the tracking measurements on the LH_2 target, the rate on the VDC was only ~300 Hz. This was more than two orders of magnitude lower than the corresponding rate on the HDC chambers, which experienced high rates from Møller scattering on the LH_2 target. These Møller electrons were swept away by the QTOR spectrometer and did not contribute to the rate observed in the VDCs. A typical residual showing the VDC position resolution achieved during these nominal running conditions is shown in Fig. 30.

9.2.1. VDC positioning system

The VDCs were located downstream of the QTOR magnet, and upstream of the main detectors. Each of the two octants was covered by a pair of chambers which constituted an arm.

In a vertical drift chamber, for which an ionizing track should typically fire about six wires per wire plane, the optimal incident track angle with respect to the wire planes is about 45°. Given the 22.5° average lab angle of the elastic scattered electrons after the QTOR magnet, the VDC pairs needed to be held at 24.4° from the vertical (optimized via GEANT [89] simulation). Each pair of VDCs in an arm was held in place at this angle by two 2.54 cm thick stainless steel side plates. Each VDC pair was separated by 53 cm (center-to-center) in the beam direction, and the center of the pair was located 107 cm upstream of the main detectors.

The two arms, held 180° apart, were mounted on rails which were in turn mounted to a central rotating hub. The positioning system allowed the 1100 kg VDC assemblies on each arm to be retracted from the acceptance (linear motion) during integrating-mode running, and rotated to cover different pairs of octants during event-mode running. Each arm could cover one of the five different octants, meaning that all eight octants could be covered, and that one octant pair could be covered by either arm (at different times) for systematic studies.

Pins locked the chambers in their retracted or extended positions. The linear and rotation motions were both automated. An electric cylinder [98] with an S6961 controller [99] was used for the linear motion. The rotation was done using a Sumitomo Drive Technology motor [100] with a HF-320 α controller [101] which drove a chain surrounding the central hub. Positioning reproducibility was better than 3 mm (azimuthal) and <1 mm (radial).

9.2.2. VDC electronics

Custom-made preamplifier/discriminator cards employing the CERN MAD chip [102,103] were mounted directly to the VDCs. The LVDS[61] output of these cards was carried through 16-channel ribbon cables 15 m long which absorbed the rotation and translation of the VDCs. Thirty meters of twisted pair fixed cables then carried the 558 signals from each VDC to a level translator in a shielded electronics hut in the experimental hall.

The level translator converted the LVDS signals to ECL[62] signals which were split into two signals. These formed the inputs to a novel digital delay multiplexing system [104]. Delayed signals from every eighth wire in a group of 141 wires were ganged together, enabling a significant reduction (factor of ~9) in the number of readout channels required. The arrival time of the multiplexed VDC signals [104] with respect to the trigger scintillators (see Section 9.3) was measured and digitized with one F1TDC module [94] per VDC.

9.3. The trigger scintillators

Plastic scintillators were used to provide the fast timing trigger to the electronics for event mode readout. The scintillators were also used in the analysis of event mode data to study neutral backgrounds in the detectors.

The trigger scintillators were 218.45 cm × 30.48 cm × 1.00 cm Bicron BC-408 plastic [105] manufactured by Saint Gobain [73]. One scintillator was positioned on each arm of the VDC rotator directly downstream of the VDCs. Light guides on each end of the scintillator were formed from strips of UV-transparent lucite coupled to

[60] Charge coupled device.

[61] Low-voltage differential signal.

[62] Emitter coupled logic.

UV-transparent disks. Photonis XP-4312B 7.6 cm diameter PMTs were coupled to the 7.6 cm diameter UV-transparent disks, and a Photonis VD123K transistorized voltage divider was used with a 3 M Ω resistance. The PMT high-voltage was set between −1725 and −1860 V.

A CAEN N842 8-channel constant fraction discriminator [106] was used in conjunction with a CAEN V706 16-channel meantimer module [107] for optimum timing performance. The efficiency of the scintillators was >99%, and the measured timing resolution using cosmic rays was ∼460 ps (RMS).

9.4. Track reconstruction software

The offline track reconstruction software was used to determine the scattered electron kinematics. This was done by comparing the straight-line track segments before (from the HDCs) and after (from the VDCs) the known spectrometer toroidal magnetic field. The overall algorithm was patterned after that developed by the HERMES collaboration [108].

Standard procedures [109] were used to convert the drift time measurement to drift distance for each wire hit in the tracking chambers. For the VDCs, individual wire-by-wire timing offsets were determined from the measured scattered electron tracks. A common timing offset was adequate for the HDCs. For the VDCs, the difference in times between the two ends of the digital delay lines was used to demultiplex and identify the wire number of each wire fired.

Once hit locations were determined, a pattern recognition algorithm was used to separately identify valid line segments in the HDCs and in the VDCs. The algorithm used a template matching scheme, similar to the one developed for the ARGUS experiment [110]. The templates were based on two-dimensional projections of a track segment. The pattern of wire hit locations was compared to a series of templates, each of progressively finer spatial resolution, which were generated from simulated tracks. Each template was stored as a bit pattern, with the spatial region of the hit stored as a "1" and regions without a hit as a "0". These allowed the construction of a searchable tree of valid patterns [111], which could be quickly and efficiently compared to the pattern corresponding to the observed wire hits.

Once a valid template was found for the wire hits corresponding to a given wire plane orientation in a given set of chambers in each arm (*X*, *U*, *V* for the HDC pair, *U*, *V* for the VDC pair), the data from each orientation was combined in a least-squares fit to form a three-dimensional track segment. Fig. 31 shows tracks from the VDCs projected to the main detectors, which compares well to the corresponding Fig. 28 provided by the focal-plane scanner in Section 8.5.

The track segment determined before the magnet from the HDCs was then "swum" numerically through the magnetic field using a fourth-order Runge–Kutta [112] procedure. This requires an initial estimate of the energy of the scattered track; this estimate was derived from the known beam energy, the scattering angle from the initial track segment, and the assumption of two-body kinematics for elastic scattering. If the resulting track after swimming through the field matched, within crude limits, the location and the angle of the actual track segment found in the VDCs, the event was accepted as valid. The scattered energy was then iteratively improved using the Newton–Rapheson method, by comparing the radial (dispersive direction) position of the VDC track with that of the swum track, and repeating the swimming process until convergence.

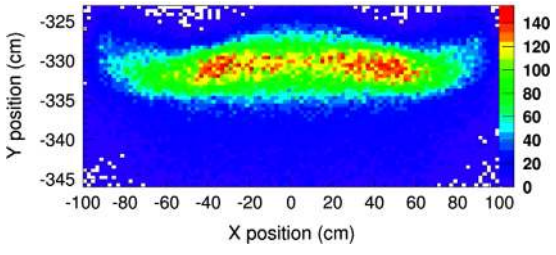

Fig. 31. A projection of tracks found in the VDCs to the main quartz detector in the bottom octant. The trigger used for these events did not include the 2 m wide main detector itself, which extended from −326 cm to −344 cm in *Y*. The *X*-axis is in horizontal direction, the *Y*-axis is in vertical direction. The scale indicates the relative electron flux.

10. Electronics and data acquisition

The DAQ[63] was built to function in one of two modes: "integrating mode" or "event mode" (see Section 1.5). Integrating mode was used with beam currents up to 180 μA to record the average detector and beamline instrumentation signals in each interval of stable beam helicity. Event mode was used with beam currents well below 1 μA to record trajectory information for individual particles in the spetrometer, triggered by a hit in one of the detector elements. The two operational modes were largely independent, but some instrumentation was common, such as the focal plane scanner (see Section 8.5).

10.1. Integrating mode preamplifiers

Low-noise pre-amplifiers based on the OPA2604 [113] and OPA2227 [114] by Burr–Brown were used to convert the Cherenkov main quartz detector anode currents to voltage signals. The pre-amps were designed [32] with two I-to-V[64] channels per RF shielded package. The transimpedance was selectable using an internal switch from 0.5 to 4.0 MΩ for the main detectors and downstream lumis and 0.5 to 50 MΩ for the upstream luminosity monitors. The output dynamic range of ±10 V was matched to the input range of the ADC (see below) and drove 130 m of RG-213 cable. A ganged output offset was internally adjustable in the range ±1.2 V. The pre-amp required a +5 V supply. An internal DC–DC converter stepped up the supply voltage to ±15 V while providing isolation from the external power supply. A 26 kHz bandwidth filter was applied to the output signals using a single pole filter. Because the detector signals were normalized to beam current, a 26 kHz filter was also used on the BCMs.

Before the experiment, a prototype pre-amp was tested to 18 krad in the mixed electron and photon field of the JLab ^{137}Cs irradiation facility with no increase in noise. During the experiment, the pre-amps were located within a few meters of the detectors and received an estimated dose of at least 1 krad from mostly electromagnetic background. No noise degradation was observed.

In integrating mode, low-capacitance RG-62 (93 Ω) cable was used to carry the anode current signal from the PMT bases to the preamplifiers. In event mode, standard RG-58 (50 Ω) cable was used. Under nominal operating conditions, all main detector pre-amps were set to 2 M Ω transimpedance, then the main detector PMT HVs were adjusted until the average signal magnitude was 6 V. At the corresponding anode current of 3 μA, the PMTs showed a modest gain drop of only ∼10% throughout the experiment (see Fig. 25). Further details, including a schematic diagram, can be found in [72].

10.2. Integrating mode instrumentation

The goal of the integrating-mode instrumentation was to record the integrated signals or yields from all the detectors and beam monitors during each period of stable beam helicity T_{Stable}, as well as recording the beam helicity itself. Most detector and beamline instrumentation signals were transformed into time-dependent voltages, and the average voltages were measured during the T_{Stable} interval by

[63] Data acquisition.
[64] Current to voltage.

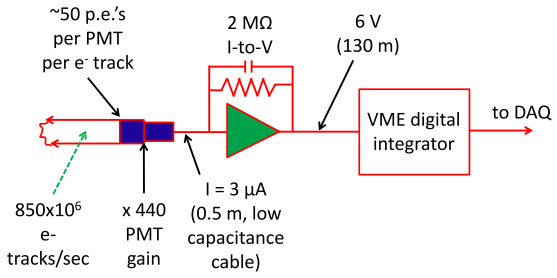

Fig. 32. A simple schematic of the main detector signal chain.

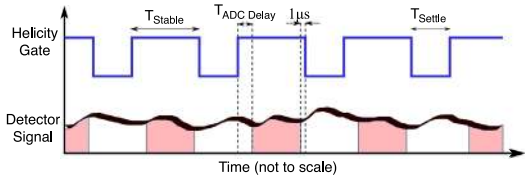

Fig. 33. The readout timing diagram of the integrating-mode DAQ. The shaded area in the detector signal indicates the signal region digitized by the ADCs. The horizontal axis scale is exaggerated to show details of the signal timing. Further information on the helicity signal timing is summarized in Fig. 5.

either a sampling-integrating ADC (the VQWK[65] modules built by TRIUMF[66] [32]) or by a gated scaler counting the output of a voltage-to-frequency converter. For a few detectors, such as the halo detectors (see Section 3.6), the instrumentation was a gated scaler counting pulses from a discriminator. The main detector signal chain is depicted schematically in Fig. 32.

The voltage signals produced by the detector and beam monitor I-to-V pre-amplifiers, as well as voltage signals produced by the BCM receivers, were digitized in the VQWK [32] ADCs. Each of the eight input signals of a VQWK module was sampled at 500 kHz by an AD7674 18-bit ADC [115] accepting a full-scale range of ± 10 V. An FPGA on the VQWK module synchronized and accumulated the sample readings into the reported value. For each gate trigger, the VQWK module accumulated a preset number of samples to produce the reading for that trigger; in addition to the total sum, four sub-sums were accumulated representing each quarter of the gate. The input stage of the VQWK module had a 5-pole low-pass filter with a 50 kHz cutoff to prevent aliasing of the input signals.

As discussed in Section 10.1, the bandwidth of the BCMs and BPMs was matched to the 26 kHz bandwidth of the integrating-mode preamplifiers. The delay of these signals was also matched, by making use of the 60 Hz pulsed (tune) beam structure available at JLab. To allow for the fact that pure analog and digital BCM receiver signals arrived out of time by $\mathcal{O}(10)$ μs, gates sent to ADC modules containing late signals were programmed to begin digitizing after a programmable delay. The flexibility to match both bandwidth and delay between the detectors and the BCMs was a crucial feature of the electronics.

At the 960/s reversal rate, the VQWK ADCs acquired 464 samples per Helicity Gate (see Fig. 5), giving a sampled average of the input voltages over a 928 μs interval. The accumulation of samples was started $T_{\mathrm{ADCDelay}} = 42.5$ μs after the beginning of the $T_{\mathrm{Stable}} = 971.65$ μs interval in the Helicity Gate signal. Thus the last sample was taken about 1 μs before the end of the T_{Stable} interval. T_{Stable} and the time set aside for the helicity transition to fully complete ($T_{\mathrm{Settle}} = 70$ μs) were set by the polarized source helicity board (see Section 2.1). T_{ADCDelay} was set internal to the VQWK modules, and was used to prevent distortion of the voltage samples by the beginning of the gate signal. The use of the T_{ADCDelay} contributed an additional 4.1% deadtime on top of the 6.7% deadtime associated with T_{Settle} discussed in Section 2.1. The readout timing diagram of the integrating-mode DAQ is summarized in Fig. 33.

The RMS width of the quartet asymmetry generated on a channel digitizing a constant voltage signal (from a battery) was about 3 ppm, compared to the ~ 230 ppm RMS width of the detector asymmetries. The random noise introduced by the electronics chain was thus negligibly small compared to the fluctuations from counting statistics.

A set of three SIS3801 [116] scalers and one STR7200 [117] scaler were used to provide rate measurements for detectors and monitor channels that were not instrumented by the VQWK modules. During the integrating-mode running, only the Helicity Gate triggers were collected; all other trigger types (see next section) were disabled. There were 32 VQWK modules in three VME crates, providing digitization of the detectors as well as beamline instrumentation in Hall C and the injector. Two additional VME crates supported the scalers and the trigger control electronics.

The total data rate was about 6.5 MB/s. The data were written to disk as a series of data files with a maximum size of 1.9 GB. These files, known as "runlets", each represented about 5–6 min of data collection. A typical hour-long run would consist of about 10–12 runlets. The analysis also benefited from the segmentation into runlets, as beam and experimental conditions were generally stable on a 5 min time-scale, but could vary more over the course of an hour-long run.

10.3. Event mode instrumentation

In event mode, detector information was collected based on detector-based triggers, as opposed to the periodic helicity-based triggers collected in integrating mode. Pre-scaling and trigger selection was done by a JLab Trigger Supervisor module [118], with several trigger inputs. The helicity-based trigger was replaced by a slower (usually 10 Hz) clock, to control readout from scalers. The most common trigger sources were the trigger scintillators, the main Cherenkov detector bars, the focal plane scanner, and one of the "background" detectors. Occasionally other trigger sources were used for tests and background measurements.

The instrumentation was changed for event mode as well. All the drift chambers were read out using JLab F1TDC modules [94]. The main detectors and trigger scintillator signals were passively split, with one copy being discriminated and input to F1TDC modules, and the other copy passing through an additional 190 ns of delay cable before being input to a CAEN V792 [119] charge-to-digital conversion (QDC) module. All the timing signals from the scintillators and Cherenkov detectors were also input to scalers.

11. Software

Simulations were performed based on the GEANT3 [120], GEANT4 [89,90] and GARFIELD [121] simulation packages. GEANT3 simulations were used in the design phase of the experiment to optimize the acceptance, and to study background from the aluminum target cell and other sources. GEANT4 was used to maximize the photoelectron yield from the quartz main detectors, and in the analysis of tracking data (see Section 9). GARFIELD was used in the design of both the horizontal and vertical drift chambers to optimize the gas mixture, field and sense wire positions, and the cathode plane spacing.

The physical processes implemented in both GEANT simulations included all electromagnetic and low-energy hadronic processes above a threshold value. In addition, generators were written for elastic $e-p$, inelastic $e-p$, and Møller scattering in the target, and for scattering from the aluminum target windows.

[65] Q_{weak} 18-bit sampling ADC.
[66] TRI-University Meson Facility.

11.1. Acceptance, rate, and momentum transfer simulations

As part of the Q_{weak} acceptance optimization, the collimator design, the position of the main detector quartz bars, and the current setting of the QTOR magnet were varied. First, the maximum solid-angle acceptance that would clear the QTOR spectrometer support structure was found. Then, for a given collimator design, the elastic rate, mean Q^2, uncertainty on Q_w^p, and the background dilution (contamination) from inelastic and target window scattering were calculated as a function of the main detector radial position. The final combination of magnetic field and detector position chosen was an optimization that minimized the Q_w^p uncertainty, through a trade-off maximizing the elastic rate and acceptance while minimizing the inelastic and target window background dilutions.

11.2. Background simulations

In addition to aiding in the design and optimization of the acceptance-defining collimator, the Q_{weak} GEANT3 [120] simulation was also used in the design of the upstream shielding wall of the detector hut, the "lintel" collimators, and the general study of backgrounds from the target windows and the beamline, as well as other background processes.

An example of one of the many improvements to the experiment's design that came out of these studies is the lintels alluded to in Section 6.2. The simulations [66] showed that electrons from elastic and Møller scattering generated photons along the inner edge of the defining collimator apertures which had direct line of sight to the detectors. Lead "lintel" collimators were added between the coils of the magnet to provide line-of-sight shielding between the Cherenkov detectors and the photons from this background source. Simulations showed that the lintels reduced this background by about 90%. Elastically scattered electrons which passed through the defining collimator apertures were deflected by the spectrometer field and not affected by the lintels. The lintels were also designed to avoid the intense "fountain" of low-energy electrons from Møller scattering in the target, in order to prevent them from becoming a net source of photon background.

The apertures in the upstream wall of the detector shielding hut were also carefully designed with GEANT3 simulations [66]. These apertures essentially constituted a fourth collimator, the only one downstream of the spectrometer magnet. Backgrounds from the aluminum target windows, beamline, collimators, and shielding wall were all studied with simulations. The results were used to devise methods to measure and suppress these backgrounds.

11.3. Detector simulations

The detector simulation software was developed [72] based on the GEANT4 [89] framework. The basic method was to track particles from the target to the detectors using the detailed geometries of the detectors and shielding as well as the measured magnetic field of the spectrometer as an input. By turning on all relevant physics processes along the particle trajectories, the detector response (light production and transport) could be simulated for various trial geometries. The simulation results were benchmarked by comparing them to independent experimental results wherever possible and the resulting deviations were then used to modify the simulation code until consistent results were obtained or a reasonable uncertainty could be assigned to the simulation results. The detector design was optimized through several such iterations.

The detector geometries were implemented in particular detail, including the quartz bars, glue joints, lightguides, PMTs, detector housing, PMT housing, PMT lead shield, pre-radiator, quartz bar holders and detector windows (covers). Relevant material properties were included, such as wavelength spectra, index of refraction, surface reflectivity of the PMT photocathode, and the quartz surface roughness. The simulation investigated the consequences of possible defects, such as a small mismatch between two quartz bars, quartz bar and/or light guide misalignment, and oversized bevels or chipped edges. Detector geometries such as detector thickness, pre-radiator thickness, and light guide shape were studied by turning on the Cherenkov process to determine the overall efficiency of the detectors for various design choices.

Extensive simulations were performed to study effects of quartz bar surface properties, to determine quartz bar and light guide shapes, quartz bar tilt angle, to study the position dependence of the light yield, as well as to study background and the Q^2 distribution in the detectors. The length (200 cm) and width (18 cm) of the quartz bars were determined by the elastic beam spot size on the focal plane. The thickness (1.25 cm) was optimized using simulations by balancing the competing aspects of maximizing light yield and minimizing shower activity and background [72]. A similar procedure was performed to find the optimal thickness (2 cm) for the pre-radiator.

The optimal Cherenkov detector light guide geometry was determined by simulating the light yield for various configurations, such as with the PMT on the edge or on the face of the light guide for rectangular, trapezoidal, or wedge guide geometries, or without a light guide (PMT on the active quartz volume edge only). Although the geometry variations showed no significant effect on the excess noise due to light yield variations, the mean photoelectron yield was largest with the PMT on the face of a rectangular light guide.

The detector tilt angle was also optimized by determining the excess noise as a function of detector tilt angle, the light yield uniformity as a function of electron hit positions along the length of the quartz bar and tilt angle, as well as the uniformity of the Q^2 distribution across the quartz bar. The light yield was smaller for a zero tilt angle, but significantly more uniform. The optimal tilt angle chosen was zero – perpendicular to the beam direction.

The simulation studies showed that the total light yield in the detector depended on the position of the incident electron – a combined effect of the shower activities in the quartz bar, the various path lengths of the electrons in the quartz bar, and the various light transmission distances in the quartz bar. The light yield was approximately uniform in the short, radial dimension but nonuniform in the long (200 cm) direction of the quartz bar. This hit position dependence of the light yield affected the excess noise in the detector as well as the light-weighted $\langle Q^2 \rangle$ determination. Because events near the middle of the quartz radiator had a lower light yield and the lower Q^2 events were focused in the center of the detector, the combination of the two effects biased the Q^2 upward by about 1.5%.

The prediction of a GEANT4 [89] simulation is compared to the measured pulse-height observed in a detector bar in Fig. 34. The measured spectrum corresponds to the sum of the signals from both ends of a pre-radiated detector bar during event mode-running at $\sim$50 pA with the LH_2 target, calibrated in photoelectrons. The simulation includes all the details of the bar described above and does an excellent job describing the measured spectrum.

11.4. Analysis software

Software was developed in C++ to decode raw data from the Q_{weak} DAQ in integrating and event modes for multiple detector systems. The DAQ integrated over the fundamental 960/s helicity window, and computed asymmetries for each helicity quartet.

After decoding of the detector signals, basic data quality cuts were applied based on the beam current and position, whether the signal was saturated, and hardware error checks. Asymmetries were then formed for the main detector (blinded), luminosity, and beamline monitors. The results were provided to ROOT [122] trees and histograms as well as to a MySQL [123] database.

In event mode, the analysis software decoded scaler, ADC, and TDC information presented by different types of triggers. The

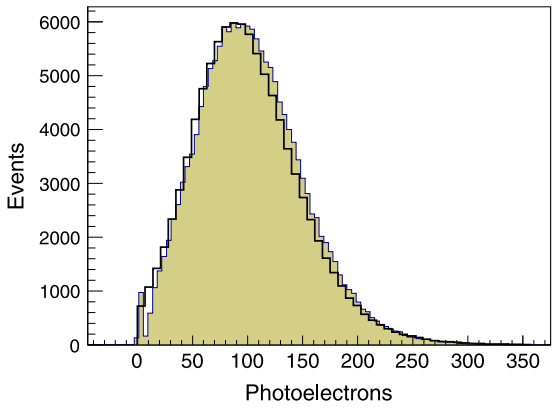

Fig. 34. *Shaded*: A typical quartz detector pulse-height spectrum accumulated during event-mode running (see text). The solid curve indicates the prediction from a GEANT4 [89] simulation incorporating the geometry of the bar and accounting for all the physical properties of the detector bar and physics processes described in the text.

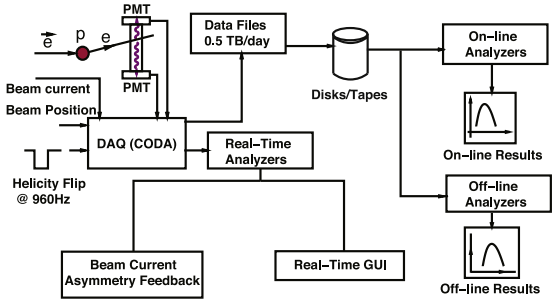

Fig. 35. The basic setup used for the DAQ and analysis framework. The DAQ generated the raw data while the analysis framework provided realtime and offline data analysis capability.

output was accessible from a set of ROOT [122] trees. An overview of the Q_{weak} data analysis system integrated with the Q_{weak} DAQ is shown in Fig. 35.

11.4.1. Online analysis

The main goal of the online analysis system was to provide a means to assess the health of the Q_{weak} DAQ and the various detector systems, as well as to assess beam quality and provide feedback to the accelerator operators. The online analysis was derived from the main analysis framework to access the DAQ in real-time and monitor the experiment's status. The monitoring system provided real-time access to a small number of important quantities. A second monitoring system summarized data quality for a much fuller set of observables from the first 5 min of each hour long run. Those results were available about half an hour after they were acquired, passed to a ROOT [122] file and used to update snap-shots to a web-based log system. An additional role played by the online analysis was a beam current asymmetry feedback loop to converge the beam charge asymmetry to zero (see Section 3.2).

11.4.2. Offline analysis

The offline analysis chain for the integrating-mode data consisted of two stages. First, the raw data files were processed to produce helicity-averaged yields and helicity-correlated asymmetries for each quartet. Then the correlations between the detector asymmetries and beam parameter variations were determined and used to correct the detector asymmetries, as described in Section 3.5.

The first step in processing the raw data was to apply calibrations to the raw detector information for each 960/s helicity gate. Several event cuts were also applied for each helicity gate: the beam current had to be above a certain threshold (usually 100 μA) and none of the main detector channels or the most important beam monitor channels could have a fault in the event. Next, a 4000-event ring buffer was used to apply a stability cut on the beam current and on two main detector channels; if the RMS of the distribution was outside of limits, all the events in the buffer were discarded. Also, if the beam current dropped abruptly, a fixed number of events before the drop were discarded.

Quartet asymmetries and helicity-averaged yields were calculated for the events that passed the event cuts and stability cuts. The main detector asymmetries were blinded by an additive shift in the asymmetry. The helicity-averaged yields and helicity-correlated asymmetries were then output to ROOT [122] files and accumulated totals were stored in a MySQL [123] database for each 5-min runlet.

Two different techniques were used to determine the correlation of the detector signals to the beam parameters. The first used linear regression analysis of the natural beam motion in each 5-min runlet to determine the correlation matrix between the detector asymmetries and the HC variation in a set of beam parameters. The matrix was then inverted to extract the sensitivity to those beam parameters for each detector. Then the detector asymmetries were corrected for the HC variation in the beam parameters, using the sensitivities extracted from that runlet. A total of 13 different sets of independent parameters were used to evaluate the effect of choosing different beam monitors on the corrected detector asymmetries.

The second method to determine the correlation of the detector signals to the beam parameters used driven beam modulation data, as described in Section 3.5. One advantage of these driven modulations was that they were largely uncoupled. In particular, the beam modulation allowed separation of the effects of energy and steering changes which were difficult to extract from the natural beam motion data.

12. Summary

As discussed in this paper, high-precision parity-violation measurements offer unique challenges from both a methodology and a technical perspective. The apparatus is essentially the entire accelerator complex, consisting of the polarized injector, accelerator, beam property measurement apparatus, scattering target, spectrometer, and detector assembly. The small asymmetries and high precision characterizing these experiments inevitably lead to high-luminosity and high-rate environments, where data are typically recorded for each helicity state as opposed to a trigger based on each scattered electron. Detector multiplicity is important to increase the detected rate, as well as to form an azimuthally symmetric array to reduce systematic errors from HC changes in the beam trajectory and potential contamination from transverse asymmetries.

The Q_{weak} experiment achieved a number of notable technical milestones. These include the highest luminosity, highest beam current on a cryogenic target, and the smallest absolute precision ever achieved in a PVES measurement. It was the first PVES measurement that required a multi-kilowatt LH_2 target that, if not for its unique design via computational fluid dynamics simulations and the use of rapid helicity reversal, would have been a limiting noise source for the measurement.

The final metric of both the instrumentation and the methodology is the degree to which all sub-systems were able to perform together at the required level. Fig. 36 illustrates the consistency of the experiment's measured asymmetry, where the sign of the various fast and slow helicity flips has been properly accounted for. These results include a global, additive blinding factor so they cannot as yet be compared to predictions. They also are not yet corrected for beam polarization, target window background, or various other small backgrounds and kinematic corrections. However, one clearly sees that

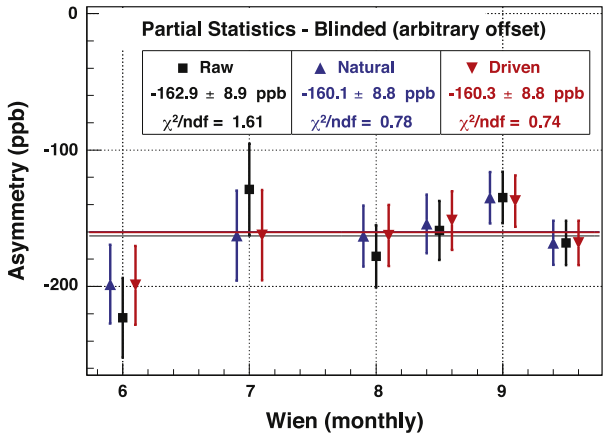

Fig. 36. Subset of the Run 2 production data showing the blinded asymmetry (in ppb) grouped by ($\sim$ monthly) the Wien state and corrected using two different approaches to determine the sensitivities of the apparatus to HC beam properties that can give rise to false asymmetries. Other needed corrections are not applied to the data in this figure, as discussed in the text. The results without any correction (solid squares) are compared to the results after correction using the intrinsic random variations in beam properties (*natural motion*: upward pointing triangles) and to the results using the driven beam motion (*driven motion*: downward pointing triangles) discussed in Section 3.5 where the sensitivities are derived by actively modulating each property of the beam with a magnitude significantly larger than intrinsically carried by the beam. The asymmetries derived using each technique are consistent with each other, and the overall correction for HCBAs is small. The data shown here represent the 80% of Run 2 data for which driven motion was available. Run 1 provides an additional $\sim 1/3$ of the total data acquired in the experiment.

the corrections to the asymmetry due to HC variations in the beam parameters are quite small, and that they are consistent for the two independent methods used to determine the sensitivities to the beam parameters (natural beam motion and driven beam modulation, as described in Section 3.5). It is also seen that the extracted asymmetry is stable with time over the scale of months. The results are evidence that the Q_{weak} physics asymmetry measurement is fundamentally sound at the few parts per billion level.

Acknowledgments

This material is based upon work supported by the U.S. Department of Energy, Office of Science, Office of Nuclear Physics under Contract DE-AC05-06OR23177, under which Jefferson Science Associates, LLC, operates Thomas Jefferson National Accelerator Facility. Construction and operating funding for the experiment was provided through the US Department of Energy (DOE) under contract number DE-AC05-06OR23177, the Natural Sciences and Engineering Research Council of Canada (NSERC), the Canada Foundation for Innovation, and the National Science Foundation (NSF) under grant numbers PHY-0320942, PHY-0321197, PHY-0320759, and PHY-0320832. University matching contributions associated with the NSF grants were received from the College of William and Mary, Virginia Tech, George Washington University, and Louisiana Tech University. We wish to thank the staff of JLab, TRIUMF, and MIT/BATES for their vital support during this challenging experiment. In particular we wish to thank the many technical and operations staff at Jefferson Lab, without whose expertise and support the experiment would not have been possible. We are grateful to A. Kenyon for his skillful guidance of the experiment's installation. We acknowledge helpful contributions from William and Mary students J. Bufkin, C. Capuano, E. Epperson, G. Giovanetti, A. Gvakharia, L.J. Snow, B.P. Walsh, and A. Watson, Virginia Tech students J. Hoffman and J. Walters, Hendrix College students D. Cargill, V. Gammill, K. Garimella, U. Garimella, N. Heiner, E. Holcomb, R. Leonard, T. Pote, G. Trees, S. Webb, and T. Webb, and University of Manitoba student C. Koop. We are also indebted to P.G. Blunden, J. Erler, N.L. Hall, W. Melnitchouk, M.J. Ramsey-Musolf, and A.W. Thomas for many useful discussions.

References

[1] R.D. Carlini, et al., The Q_{weak} Experiment: A Search for New Physics at the TeV Scale via a Measurement of the Proton's Weak Charge, JLAB-PHY-12-1478, arXiv:1202.1255, 2007.
[2] D. Androic, et al., Physical Review Letters 111 (2013) 141803.
[3] J. Erler, A. Kurylov, M.J. Ramsey-Musolf, Physical Review D 68 (2003) 016006.
[4] C.S. Wood, S.C. Bennett, D. Cho, B.P. Masterson, J.L. Roberts, C.E. Tanner, C. E. Wieman, J. Erler, A. Kurylov, M.J. Ramsey-Musolf, Science 275 (1997) 1759.
[5] N.L. Hall, P.G. Blunden, W. Melnitchouk, A.W. Thomas, R.D. Young, Physical Review D 88 (2013) 013011.
[6] R.D. Young, R.D. Carlini, A.W. Thomas, J. Roche, Physical Review Letters 99 (2007) 122003.
[7] D.T. Spayde, et al., (SAMPLE), Physics Letters B 583 (2004) 79.
[8] T.M. Ito, et al., (SAMPLE), Physical Review Letters 92 (2004) 102003.
[9] K.A. Aniol, et al., (HAPPEX), Physical Review Letters 82 (1999) 1096.
[10] K.A. Aniol, et al., (HAPPEX), Physical Review Letters 96 (2006) 022003.
[11] K.A. Aniol, et al., (HAPPEX), Physics Letters B 635 (2006) 275.
[12] A. Acha, et al., (HAPPEX), Physical Review Letters 98 (2007) 032301.
[13] Z. Ahmed, et al., (HAPPEX), Physical Review Letters 108 (2012) 102001.
[14] D.S. Armstrong, et al., (G0), Physical Review Letters 95 (2005) 092001.
[15] D. Androić, et al., (G0), Physical Review Letters 104 (2010) 012001.
[16] F.E. Maas, et al., (PVA4), Physical Review Letters 93 (2004) 022002.
[17] F.E. Maas, et al., (PVA4), Physical Review Letters 94 (2005) 152001.
[18] S. Baunack, et al., (PVA4), Physical Review Letters 102 (2009) 151803.
[19] C.W. Leeman, D.R. Douglas, G.A. Krafft, Annual Reviews of Nuclear Particle Science 51 (2001) 412.
[20] M. Poelker, et al., AIP Conference Proceedings 980 (2008) 73.
[21] P.A. Adderley, et al., Il Nuovo Cimento C 035N04 (2012) 152.
[22] OC-100-HG Opto-Coupler, Voltage Multipliers, Inc., URL ⟨http://www.voltagemultipliers.com⟩.
[23] Behlke Power Electronics GmbH, Kronberg, Germany, URL ⟨http://www.behlke.com⟩.
[24] R. Silwal, Probing the strangeness content of the proton and the neutron radius of 208Pb using parity-violating electron scattering (Ph.D. thesis), University of Virginia, Charlottesville, VA, 2012, URL ⟨https://misportal.jlab.org/ul/publications/view_pub.cfm?pub_id=12072⟩.
[25] P.A. Adderley, J. Clark, J. Grames, J. Hansknecht, K. Surles-Law, D. Machie, M. Poelker, M.L. Stutzman, R. Suleiman, Physical Review Special Topics: Accelerator Beams 13 (2010) 010101.
[26] C.K. Sinclair, P.A. Adderley, B.M. Dunham, J.C. Hansknecht, P. Hartmann, M. Poelker, J.S. Price, P.M. Rutt, W.J. Schneider, M. Steigerwald, Development of a high average current polarized electron source with long cathode operational lifetimePhysical Review Special Topics: Accelerator Beams 10 (2007) 023501.
[27] K.D. Paschke, AIP Conference Proceedings 1149 (2008) 853.
[28] J. Grames, R. Suleiman, P.A. Adderley, J. Clark, J. Hansknecht, D. Machie, M. Poelker, M.L. Stutzman, Physical Review Special Topics: Accelerator Beams 14 (2011) 043501.
[29] H. Liu, J. Bisognano, in: PAC93 Conference Proceedings, URL ⟨http://accelconf.web.cern.ch/AccelConf/p93/PDF/PAC1993_0512.PDF⟩.
[30] P.A. Adderley, et al., in: Conference Proceedings, vol. C110328, 2011, p. 862, URL ⟨http://accelconf.web.cern.ch/AccelConf/PAC2011/papers/tup025.pdf⟩.
[31] K.B. Unser, Design and preliminary tests of a beam intensity monitor for LEP, in: Proceedings of the 1989 IEEE Particle Accelerator Conference, vol. 1, 1989, p. 71.
[32] Custom Readout Electronics, Designed and Built by TRIUMF, Vancouver, Canada.
[33] Heliax Coaxial Cable, See For Example, URL ⟨http://www.rfparts.com/coax/heliaxcoax.html⟩.
[34] R. Beminiwattha, A measurement of the weak charge of the proton through parity violating electron scattering using the qweak apparatus: a 21% result (Ph.D. thesis), Ohio University, Athens, OH, 2013, URL ⟨https://misportal.jlab.org/ul/publications/view_pub.cfm?pub_id=12290⟩.
[35] T. Powers, L. Doolittle, R. Ursic, J. Wagner, Design, commissioning and operational results of wide dynamic range BPM switched electrode electronics, AIP Conference Proceedings, 390 (1997) 257.
[36] J. Musson, T. Allison, R. Flood, J. Yan, JLAB-ACE-09-975.
[37] B. Waidyawansa, A 3% measurement of the beam normal single spin asymmetry in forward angle elastic electron–proton scattering using the qweak setup (Ph.D. thesis), Ohio University, Athens, OH, 2013, URL ⟨https://misportal.jlab.org/ul/publications/view_pub.cfm?pub_id=12540⟩.
[38] C. Yan, et al., Nuclear Instruments and Methods in Physics Research A 365 (1995) 261.
[39] C. Yan, R. Carlini, D. Neuffer, in: Conference Proceedings, vol. CC930517, 1993, p. 2136.
[40] C. Yan, R. Carlini, AIP Conference Proceedings 269 (1992) 571–582.
[41] OPTIM, URL ⟨http://www-bdnew.fnal.gov/pbar/organizationalchart/lebedev/OptiM/optim.htm⟩.
[42] M. Hauger, et al., Nuclear Instruments and Methods in Physics Research A 462 (2001) 382.

[43] M. Loppacher, Møller polarimetry for CEBAF Hall C (Masters thesis), University of Basel, Switzerland, 1996.
[44] L.G. Levchuk, Nuclear Instruments and Methods in Physics Research A 345 (1994) 496.
[45] K. Halbach, R.F. Holsinger, Particle Accelerators 7 (1976) 213.
[46] Operators Manual VerdiTM V-8/V-10 Diode-Pumped Lasers. Coherent, Inc. 08/2005, Part No. 0174-929-00, Rev DB.
[47] N. Vansteenkiste, et al., Journal of the Optical Society of America A 10 (1993) 2240.
[48] D. Jones, PoS PSTP 2013 (2013) 035.
[49] R.W.P. Drever, Applied Physics B 31 (1983) 97.
[50] Hamamatsu R4885 PMT, URL ⟨http://datasheets.globalspec.com/ds/1185/Hamamatsu/3BD93D9A-7023-48C5-A511-A65FAFD354D1⟩.
[51] URL ⟨http://www.struck.de/sis3320.htm⟩.
[52] M. Friend, G.B. Franklin, B. Quinn, Nuclear Instruments and Methods in Physics Research A 676 (2012) 66.
[53] The CERN grade diamond plates were procured from Element Six, 35 West 45th St., New York, NY 10036, USA.
[54] The diamond plates were metalized and wire bonded by Diamond Detectors Limited, 16 Fleetsbridge Business Centre, Upton Road, Poole, Dorset BH17 7AF, UK.
[55] FTSH-125-04-L-DV connectors manufactured by Samtec, Inc.
[56] VME General Purpose Logic Module, v1495 manufactured by CAEN, S.p.A., Via Vetraia, 1155049 – Viareggio (LU), Italy.
[57] CODA Reference Manual.
[58] C.Y. Prescott, SLAC-TN-73-001.
[59] G.R. Smith, S. Covrig, J. Dunne, JLab Technical Design Note, JLAB-PHY-09-1313, 2009.
[60] G.R. Smith, Hyperfine Interactions 201 (2009) 57.
[61] GNB Corporation, URL ⟨www.gnbvalves.com⟩.
[62] Meyer Tool & Manufacturing, Oak Lawn, IL, URL ⟨http://www.mtm-inc.com/⟩.
[63] Sorensen DCS 60-50E 3 kW DC Power Supply, URL ⟨http://www.sorensen.com/products/DCS/DCS_Specifications.htm⟩.
[64] Lake Shore Cryotronics, Inc., URL ⟨www.lakeshore.com⟩.
[65] Baldor Electric Company, URL ⟨http://www.baldor.com/support/literature_load.asp?ManNumber=MN408⟩.
[66] K.E. Myers, The first determination of the proton's weak charge through parity-violating asymmetry measurements in elastic e + p and e + Al scattering (Ph.D thesis), George Washington University, Washington, DC, 2012, URL ⟨https://misportal.jlab.org/ul/publications/view_pub.cfm?pub_id=11273⟩.
[67] G.R. Smith, Il Nuovo Cimento C 035N04 (2012) 159.
[68] Spectrosil 2000 Fused Quartz Material Properties, URL ⟨http://www.matweb.com/search/datasheettext.aspx?matguid=9d934f588f3f44df9396996e94b61c7a⟩.
[69] D. Hasell, et al., Nuclear Instruments and Methods in Physics Research A 603 (2009) 247.
[70] P. Wang, Magnetic field simulation and mapping for the Q_{weak} experiment (Master's Thesis), University of Manitoba, Canada, 2007, ISBN:9780494359006, URL ⟨http://hdl.handle.net/1993/2454⟩.
[71] Alpha Scientific Electronics, URL ⟨http://www.alphascientific.com/⟩.
[72] P. Wang, A Measurement of the Proton's Weak Charge Using an Integration Cerenkov Detector System (Ph.D. Thesis), University of Manitoba, Canada, 2011, URL ⟨http://hdl.handle.net/1993/4835⟩.
[73] Saint-Gobain Quartz, URL ⟨http://www.quartz.saint-gobain.com/⟩.
[74] Scionix, URL ⟨www.scionix.nl/⟩.
[75] Electron Tubes ET9312 PMT, URL ⟨www.et-enterprises.com/files/file/Pmtbrochure08A.pdf⟩.
[76] Shin-Etsu Chemical Co. SES406, URL ⟨http://www.shinetsusilicones.com/content/ses-406⟩.
[77] The Nuclear Services at North Carolina State University, URL ⟨http://www.ne.ncsu.edu/nrp/services.html⟩.
[78] Stockwell Elastomerics PORON Foam, URL ⟨http://www.stockwell.com/poron-foam-cellular-urethane.php⟩.
[79] Kings Teflon, URL ⟨www.winchesterelectronics.com⟩.
[80] Alanod GmbH & Co. MIRO 27 Data Sheet, URL ⟨http://alanod.com/opencms/export/sites/alanod/en/technical_data/data_sheets/pdf/MIRO-SILVER/4270AG.pdf⟩.
[81] J. Leacock, Measuring the weak charge of the proton and the hadronic parity violation of the $N \rightarrow \Delta$ transition (Ph.D. thesis), Virginia Polytechnic Institute and State University, Blacksburg, VA, 2012, URL ⟨https://misportal.jlab.org/ul/publications/view_pub.cfm?pub_id=11932⟩.
[82] Hamamatsu Photonics, R375 PMT, URL ⟨https://www.hamamatsu.com/us/en/R375.html⟩.
[83] J. Pan, Towards a precision measurement of parity-violating e-p elastic scattering at low momentum transfer (Ph.D. thesis), University of Manitoba, Canada, 2012, URL ⟨http://mspace.lib.umanitoba.ca/jspui/handle/1993/8124⟩.
[84] Alanod GmbH & Co. MIRO 4 Data Sheet, URL ⟨http://alanod.com/opencms/export/sites/alanod/en/technical_data/data_sheets/pdf/MIRO/4400GP.pdf⟩.
[85] Lintech-Motion X-Y 90 Series Positioning System, URL ⟨http://www.lintechmotion.com/pdffiles/Lintech_90_Whole_Section_2014-01.pdf⟩.
[86] Danaher S300 Servo-Amplifier, URL ⟨http://www.kollmorgen.com/en-gb/products/drives/servo/s300/s300-servo-drive/⟩.
[87] Galil Motion Controller, URL ⟨http://www.galilmc.com/products/dmc-40x0.php⟩.
[88] ATech Linear Displacement Draw Wire Potentiometer, URL ⟨http://www.a-tech.ca/subcat.php?id=18⟩.
[89] S. Agostinelli, et al., Nuclear Instruments and Methods in Physics Research A 506 (2003) 250.
[90] J. Allison, et al., IEEE Transactions on Nuclear Science NS-53 (2006) 270.
[91] Ertalyte, URL ⟨http://www.quadrantplastics.com/na-en/products/machinable-plastics/engineering-175-325-f/ertalyte-R-pet-p.html⟩.
[92] K.B. Burns, B.R. Grummon, T.A. Nunamaker, L.W. Mo, S.C. Wright, Nuclear Instruments and Methods in Physics Research A 106 (1973) 171.
[93] Nanometric N-277 Preamplifier/Discriminator Cards, URL ⟨http://www-esd.fnal.gov/esd/catalog/main/nanomet/n-277.htm⟩.
[94] F.J. Barbosa, E. Jastrzembski, J. Prott, J. Wilson, The Jefferson Lab high resolution TDC module, in: Nuclear Science Symposium Conference Record, 2002 IEEE 1, 2002, p. 135. Piscataway, NJ, USA, http://dx.doi.org/10.1109/NSSMIC.2002.1239284.
[95] J.P. Leckey IV, The first direct measurement of the weak charge of the proton (Ph.D. thesis), The College of William and Mary, Williamsburg, VA, 2012, URL ⟨https://misportal.jlab.org/ul/publications/view_pub.cfm?pub_id=11153⟩.
[96] K.G. Fissum, W. Bertozzi, J.P. Chen, D. Dale, H.C. Fenker, J. Gao, A. Gavalya, S. Gilad, C.R. Leathers, N. Liyanage, Nuclear Instruments and Methods in Physics Research A 474 (2001) 108.
[97] G10 FR4, URL ⟨http://www.g10fr4.com/⟩.
[98] Industrial Devices Corporation Electric Cylinder Model EC3-T32V-50-05B-1000-MT4-FC2-BS24, URL ⟨http://www.tollo.com/cd/pdf/EC-MANUAL.pdf⟩.
[99] Industrial Devices Corporation S6961 Controller, URL ⟨http://www.artisantg.com/PLC/72470/Kollmorgen_IDC_S6961_One_Axis_Microstepping_SmartDrives⟩.
[100] Sumito LHHM1-3B120LKA-K1-B-249 Motor, URL ⟨http://www.sumitomodrive.com/⟩.
[101] Sumito HF-320 Controller, URL ⟨https://www.sumitomodrive.com/uploads/product/files/file-224.pdf⟩.
[102] F. Gonella, M. Pegoraro, in: Seventh Workshop on Electronics for LHC Experiments, vol. 204, 2001.
[103] F. Gonella, M. Pegoraro, CERN Technical Report, CERN, 2000.
[104] R. Zielinski, Testing and analysis of Q-weak's multiplexing electronics system (Senior thesis), The College of William and Mary, Williamsburg, VA, 2010, URL ⟨http://physics.wm.edu/~armd/RyanThesis.pdf⟩.
[105] Bicron BC-408, URL ⟨http://www.phys.ufl.edu/courses/phy4803L/group_I/muon/bicron_bc400-416.pdf⟩.
[106] Caen N842, URL ⟨http://www.caen.it/csite/CaenProd.jsp?idmod=274&parent=12⟩.
[107] Caen V706, URL ⟨https://groups.nscl.msu.edu/mona/docs/V706.pdf⟩.
[108] K. Ackerstaff, et al., (HERMES), Nuclear Instruments and Methods in Physics Research A 417 (1998) 230.
[109] L.G. Atencio, J.F. Amann, R.L. Boudrie, C.L. Morris, Nuclear Instruments and Methods in Physics Research A 187 (1981) 381.
[110] H.D. Schulz, H.J. Stuckenberg, A trigger processor for Argus, in: Proceedings of topical conference on the application of microprocessors in high energy physics experiments, CERN 81-07, 1981.
[111] M. Dell'Orso, L. Ristori, Nuclear Instruments and Methods in Physics Research A 287 (1990) 436;
P. Battaiotto, et al., Nuclear Instruments and Methods in Physics Research A 287 (1990) 431.
[112] W.H. Press, B.P. Flannery, S.A. Teukolsky, W.T. Vetterling, Numerical Recipes in C: The Art of Scientific Computing, second ed., Cambridge University Press, 1993.
[113] Burr-Brown OPA2604, URL ⟨http://www.alldatasheet.com/datasheet-pdf/pdf/56744/BURR-BROWN/OPA2604.html⟩.
[114] Burr-Brown OPA2604, URL ⟨http://www.alldatasheet.com/datasheet-pdf/pdf/56738/BURR-BROWN/OPA2227.html⟩.
[115] AD7674, URL ⟨http://www.analog.com/en/analog-to-digital-converters/ad-converters/ad7674/products/product.html⟩.
[116] Struck SIS3801, URL ⟨www.struck.de/sis3801.htm⟩.
[117] Struck STR7200, URL ⟨http://www.usatlas.bnl.gov/~poblague/doc/hw/STR7200.pdf⟩.
[118] Jefferson Lab Trigger Supervisor, URL ⟨https://coda.jlab.org/wiki/Downloads/docs/manuals/Trigger%20Supervisor%20V2.pdf⟩.
[119] Caen V792, URL ⟨http://www.caen.it/csite/CaenProd.jsp?idmod=41&parent=11⟩.
[120] J. Apostolakis, GEANT—Detector Description and Simulation Tool, 2003. URL ⟨http://wwwasd.web.cern.ch/wwwasd/geant/⟩. IEEE Transactions on Nuclear Science NS-53 (2006) 270.
[121] R. Veenhoff, Garfield—Simulation of Gaseous Detectors, 2010, URL ⟨http://garfield.web.cern.ch/garfield/⟩.
[122] R. Brun, F. Rademakers, ROOT—an object oriented data analysis framework, in: Proceedings AIHENP'96 Workshop, Lausanne, September 1996, Nuclear Instruments and Methods in Physics Research A 389 (1997) 81. See also URL ⟨http://root.cern.ch/⟩.
[123] MySQL, An Open Source Database, URL ⟨http://www.mysql.com⟩.